Title
Engineering SERS platform in fiber application with a spectroscopic study of bilayer MoS2

Author
Xia, Ming

Publication Date
2016

Peer reviewed|Thesis/dissertation

UNIVERSITY OF CALIFORNIA

Los Angeles

Engineering SERS platform in fiber application with a spectroscopic study of bilayer MoS_2

A dissertation submitted in partial satisfaction of the requirements for the degree Doctor of Philosophy in Materials Science and Engineering

by

Ming Xia

2016

ABSTRACT OF THE DISSERTATION

Engineering SERS platform in fiber application with
a spectroscopic study of bilayer MoS_2

by

Ming Xia
Doctor of Philosophy in Materials Science and Engineering
University of California, Los Angeles, 2016
Professor Ya-Hong Xie, Chair

Surface Enhanced Raman Spectroscopy (SERS) is a surface-sensitive technique based on plasmon resonance, which can enhance Raman signal intensity by several orders of magnitude, enabling even detection of a single molecule. Material topics involving SERS contain manipulation of specific hot spots through nano-fabrication and enhancement of substrate sensitivity and affinity to interested molecules. The main objective of this research is to gain fundamental understanding of capability limit of SERS optical fiber technology through systematic experimental studies combined with simulations.

SERS fiber probe based on Au nanotriangle has been fabricated and factors affecting Raman signal through fiber are investigated. These factors include numerical aperture of

objective lens, slit width of spectrometer, fiber length and SERS array size on fiber facet. Size of SERS array coated on fiber facet is one primary factor accounting for Raman signal loss, which is ultimately due to decrease in laser power density on the fiber end. The most fundamental optimization consideration for SERS fiber probe is a tradeoff between sensitivity and spatial resolution.

A novel Au pyramid/ring SERS platform with enhancement of spatial confinement and electric field is demonstrated for potential SERS fiber probe application through finite-difference time-domain (FDTD) simulation. The FDTD simulation work provides an alternative way to enhance Raman signal intensity while keep high spatial resolution for SERS fiber probe. Excitation of surface plasmon polaritons (SPPs) by circular Au rings and coupling of SPPs with Au pyramids are studied to improve electric field and overall SERS enhancement of the platform. Au pyramids combined with rings can achieve confinement of the electric field within a 700×700 nm region, which could provide higher spatial resolution for SERS fiber probe.

In addition, a practical way of patterning metallic nanostructures for achieving high SERS enhancement factors (EFs) and high hot spot density is demonstrated. By superimposing one layer Au triangle array on another to form multilayer triangle array, SERS signal can be enhanced by two orders of magnitude. The physical understanding of the SERS enhancement of multilayer triangle array is also developed through FDTD simulation. The drastic increased SERS EFs and hot spot density are due to an increase of amount of gaps formed between Au

triangles and a decrease of the gap size.

The thesis also presents a serendipitous discovery of bilayer MoS_2 spectral features when exploring MoS_2 as a potential SERS enhancement substrate. CVD grown AA' (60° stacking) and AB (0° stacking) stacked bilayer MoS_2 have distinct properties in terms of resonance Raman and photoluminescence. Raman and photoluminescence spectra of AA' and AB stacked bilayer MoS_2 are obtained on Au nano-pyramid surfaces under strong plasmon resonance. A Raman peak named as "a" peak appears in AA' stacked bilayer MoS_2 resonance Raman spectra but not in AB stacked bilayer, a feature that can be used as Raman finger print to differentiate the two types of bilayer MoS_2.

The dissertation of Ming Xia is approved.

Sotiris Masmanidis

Dwight Christopher Streit

Ya-Hong Xie, Committee Chair

University of California, Los Angeles

2016

To my parents and wife, who supported me throughout my PhD study

Table of Contents

Acknowledgments

First, I want to express my gratitude to Prof. Ya-Hong Xie, who patiently guided my research throughout all my PhD study at UCLA. Prof. Xie's abundant knowledge and altitude to scientific research benefit me a lot. Through Prof. Xie's mentorship, I not only learned how to conducted research independently, but also developed my skill set. I want to extend my gratitude to my lab mates in Prof. Xie's Group: Dr. Pu Wang, thank you for the insightful discussion about the SERS and teaching me how to use the FDTD simulation software; Dr. Wei Zhang, thank you for introducing and teaching me the nanofabrication at the Nanolab at UCLA; Owen Liang, thank you for training me to grow graphene and use Raman microscope; Pei Zhang, Zhongbo Yan, Xinke Yu, Peiyi Ye, and Jimmy Ng, thank you for the kind help in my research and the open discussions.

In addition, I want to thank the collaborators outside UCLA during my PhD research. I want to thank Dr. Bo Li at Rice University, Dr. Kuibo Yin at Southeast University, Dr. Wu Zhou at Oak Ridge National Laboratory, Dr. Gang Niu and Dr. Giovanni Capellini at IHP in Germany. Moreover, I want to thank Kuan Qiao, who was a summer research undergraduate in our group, for his help in the FDTD simulation and the experiment of multiple layered Au nanostructure.

At the end, I want to thank for the unconditional support from my wife, Yixiang Zhang. Thank you for accompanying me through my PhD study. I will never forget the happy time we spent together and how you encouraged me during the tough time in my PhD study. Last but not

least, I would like to thank my parents for their support to my choice to study abroad and pursue my dreams.

This research is supported by Function Accelerated nanomaterial Engineering (FAME), one of six centers of STARnet, a Semiconductor Research Corporation program sponsored by MARCO and DARPA. Chapter 3 is a version of " Ming Xia, Pei Zhang, Kuan Qiao, Yu Bai, and Ya-Hong Xie, Coupling SPP with LSPR for Enhanced Field Confinement: A Simulation Study, The Journal of Physical Chemistry C, 120 (2016), 527–33". Chapter 4 is a version of " Ming Xia, Kuan Qiao, Zhiyuan Cheng, and Ya-Hong Xie, Multiple Layered Metallic Nanostructures for Strong Surface-Enhanced Raman Spectroscopy Enhancement, Applied Physics Express (2016) ". Chapter 5 is a version of " Ming Xia, Bo Li, Kuibo Yin, Giovanni Capellini, Gang Niu, Yongji Gong, Wu Zhou, Pulickel M Ajayan, and Ya-Hong Xie, Spectroscopic Signatures of AA′ and AB Stacking of Chemical Vapor Deposited Bilayer MoS_2, ACS nano, 9 (2015), 12246-54".

VITA

2010	B.S. in Materials Science and Engineering
	Xi'an Jiaotong University
	Xi'an, China
2012	M.S. in Materials Science and Engineering
	Tsinghua University
	Beijing, China
2016	Ph.D. Candidate in Materials Science and Engineering
	University of California, Los Angeles
	Los Angeles, CA, USA

Publications:

1. Xia M, Qiao K, Cheng Z, et al . Multiple Layered Metallic Nanostructures for Strong Surface-Enhanced Raman Spectroscopy Enhancement. *Appl. Phys. Express*, 2016.
2. Xia M, Zhang P, Qiao K, et al. Coupling SPP with LSPR for Enhanced Field Confinement: A Simulation Study. *J. Phys. Chem. C*, 2016, 120 (1): 527–533.
3. Xia M, Li B, Yin K, et al. Spectroscopic Signatures of AA' and AB Stacking of Chemical Vapor Deposited Bilayer MoS_2. *ACS Nano*, 2015, 9 (12): 12246-12254.
4. Wang P, Xia M, Liang O, et al. Label-Free SERS Selective Detection of Dopamine and Serotonin Using Graphene-Au Nanopyramid Heterostructure. *Anal. Chem.*, 2015, 87 (20): 10255-10261.

Chapter 1 Introduction

1.1 Motivation of the Thesis

Surface enhanced Raman spectroscopy (SERS) is an important analytical technique that is able to provide single molecule detection and high resolution Raman spectral information.[1-3] Since its first discovery,[4] SERS technique has been widely used for detection of trace amount of molecules due to its high sensitivity.[5-8] Many efforts have been devoted to develop various SERS metallic (mainly Au and Ag) nanostructures to enhance Raman signal.[7, 9, 10] Although there are continuous reports of new SERS substrates in literature, few SERS techniques have been applied in the real clinical or biomedical world. Other exploration includes coupling optical fiber with SERS platform for remote and flexible biosensing.[11-13] SERS optical fiber probe is considered as a potentially practical way to extend the SERS technology into clinical application.[14] The main objective of the thesis work is to gain fundamental understanding of capability limit of SERS fiber technology through systematic experimental studies combined with simulations.

This chapter introduces background of SERS in Section 1.2, *in vivo* SERS biosensing in Section 1.3, and SERS optical fiber probe in Section 1.4 that is required for appreciation of the research presented in this dissertation. Chapter 1.5 presents the outline of the dissertation.

1.2 Surface Enhanced Raman Spectroscopy

SERS technique is based on Raman scattering process. In Raman scattering process, a

molecule absorbs an incident photon with energy E_L and is excited from ground state to a virtual state by the incident photon. Because the virtual state is not stable, the molecule will jump back to its ground state and emit a Raman scattered photon with different energy E_S. The energy difference between the incident photon and the Raman scattered photon is called Raman shift ($\Delta E_R = E_L - E_S$), which provides vibrational information of molecules. ΔE_R is positive for a Stokes and negative for an anti-Stokes process. Figure 1.1 shows the schematic of Raman scattering process (Stokes-process). Raman spectrum is wavelength- (or energy-) dependence of Raman scattered intensity at a given incident wavelength.

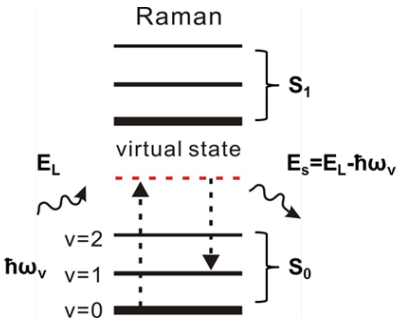

Figure 1.1 Schematic of Raman scattering process (Stokes-process).

SERS effect is about enhancing Raman signal by several orders of magnitude. There are mainly two mechanisms that explain SERS effect. One is electromagnetic (EM) enhancement mechanism, and the other is chemical enhancement mechanism. In EM enhancement, excitation light interacts with nanosized metallic SERS substrates and generates localized surface plasmon resonance (LSPR). Molecules absorbed at metallic surfaces experience a large amplification of

laser field locally due to plasmon resonance while undergoing Raman processes, and thus generate enhanced Raman signal. Majority of SERS effects are due to EM enhancement on metallic nanostructures. Chemical enhancement is mainly due to charge transfer mechanism between molecules and substrate surfaces, and the magnitude of Raman signal enhancement is very low compared with EM enhancement. Therefore, the following part of the thesis will focus on SERS effects due to EM enhancement.

LSPR generates strong local electric field near metallic surfaces, which amplifies Raman signal of molecules absorbed on metallic surfaces. Localized surface plasmon (LSP) is a photon-driven coherent oscillation of the surface conduction electrons in a material with negative real and near-zero imaginary dielectric constant.[15] Figure 1.2 shows the schematic diagram of LSP. External electric field of excitation light moves away the free electrons inside the nanosized metal spheres to one direction, creating an electric dipole. The electric dipole can switch its direction with the change of the external field. When the incident photon frequency matches the collective oscillation of dipole plasmon, resonance condition is reached, generating the strongest signal for plasmon and the strong electric field.[16] To quantify SERS enhancement effect, the concept of SERS enhancement factor (EF) was brought up. SERS EF reflects how much the Raman signal can be boosted. A commonly used approximation is that SERS EF is proportional to the fourth power of the magnitude of electric field ($|E|^4$).[17] Typical SERS EF of metallic SERS substrates is from 10^3 to 10^{14}. Various metallic (mainly Ag and Au) nanostructures [18-22] have

been developed and fabricated to achieve strong local electric field and high SERS EFs.

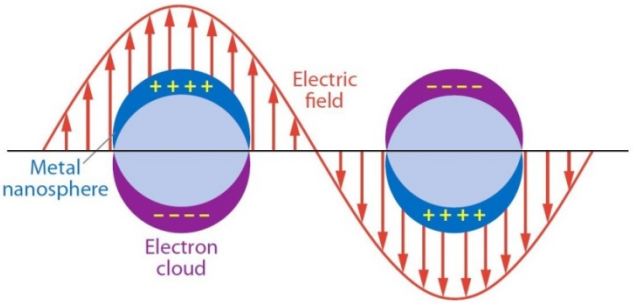

Figure 1.2 Schematic diagram illustrating a localized surface plasmon of metal spheres.[23]

1.3 SERS Biosensing for *in vivo* Application

SERS technique has been widely explored for *in vivo* biosensing due to its high sensitivity. SERS *in vivo* biosensing can be generally classified into two methods, intrinsic and extrinsic biosensing.[24] Intrinsic SERS biosensing directly provides Raman signature for analytes of interest, such as protein, DNA strand, or small molecules. Extrinsic SERS biosensing provides Raman signature of a molecule (or Raman reporter) with an intense and distinguishable Raman features, and analyte of interest is associated with this molecule. Bisosensing of target analyte is based on spectra of Raman reporter molecules. Therefore, extrinsic SERS biosensing is an indirect sensing method.

Intrinsic SERS biosensing is also known as lab-free SERS biosensing sometimes. In label-free SERS biosensing, SERS substrates contact with target anlayte and generate strong SERS signal, which is used to identify interested molecules or do quantification. There is few study of applying label-free SERS in *in vivo* system. The Van Duyne group[25] first demonstrated

in vivo label-free SERS detection of the glucose from the interstitial fluid of a rat. The SERS substrate used in this study was the silver film over nanosphere (AgFON) functionalized with a self-assembled monolayer (SAM). The SERS substrate was implanted under the skin of a rat in a way that the fluid was in contact with the SERS metallic surface and the laser was focused on the SERS substrate through a glass window. One major advantage of label-free SERS is that it can provide rich spectroscopic information for detection and identification without labeling, and thus reduce the time for detection. The disadvantages of label-free SERS include the lack of specificity and the difficulty of identifying analytes from the spectroscopic information for large biomolecules, like proteins and DNA.

Compared with intrinsic or label-free SERS, extrinsic SERS is widely explored for *in vivo* biosensing. Extrinsic SERS relies on SERS nanoparticle tags (or nanotags) to identify analyte of interest. A SERS nanotag contains a metal nanoparticle core, Raman reporters on the metal surface, and a biocompatible layer which encases the metal particle and Raman reporters, as shown in Figure 1.3. Commonly used biocompatible layers are polyethylene glycol (PEG) and silica, which maintain colloidal stability and prevent interaction of the Raman reporter with the external environment. This biocompatible layer can then be further functionalized with targeting agents toward specific receptors. The targeting agents on the nanotags will provide the detection specificity through binding on the receptor on the target anlaytes. When the SERS nanotags accumulate on the analyte (e.g. cells), Raman signal of Raman reporter molecules can be

enhanced and detected. Biosensing of the analyte is achieved through measuring the Raman signal of reporter molecules. SERS nanotags have been used for *in vivo* tumor detection in mouse.[26] Nie and co-workers[26] used functionalized Au nanoparticles as SERS nanotags to identify tumor in mouse. After injecting NPs into the mouse from the tail vein, SERS signal could be detected from a targeted tumor site up to 2 cm below the skin. The major advantage of using SERS nanotags is that extrinsic Raman reporter molecules can overcome background signals from a complex biological matrix and associate with specific biomolecules.

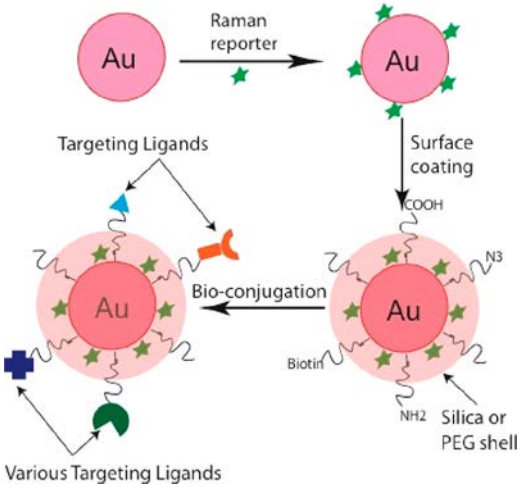

Figure 1.3 Structure of biofunctionalized SERS nanoparticle tags, consisting of a metal nanoparticle core, adsorbed Raman reporters on the metal surface (green stars), a biocompatible layer (orange layer), and targeting ligands.[27]

1.4 SERS Optical Fiber Probe

SERS optical fiber probe is a technique combing the sensitivity of SERS substrate and the flexibility of optical fiber. The most widely employed SERS optical fiber geometry is to couple

the SERS substrate on a fiber end, as indicated in Figure 1.4. The single fiber serves two functions, one is to guide the excitation laser to the targeting analytes, and the other is to collect the SERS signal generated on the fiber end and guide the signal to the spectrometer. This single ended measurement geometry is also referred as "optrode" sometimes. Compared with labeled nanoparticles, SERS optical fiber probe with single ended measurement geometry has been gaining attention for *in vivo* label-free biosensing due to their flexibility and compatibility with remote sensing. The advantages of SERS fiber probe over labeled SERS nanotags for *in vivo* biosensing lie in two aspects. First, label-free SERS fiber detection scheme allows real-time detection and eliminates time and cost consuming labeling procedures. [28] Second, SERS fiber detection provides the ability of remote and flexible sensing. SERS fiber probe also suffers from the interference from fluorescence and Raman background of fiber itself.

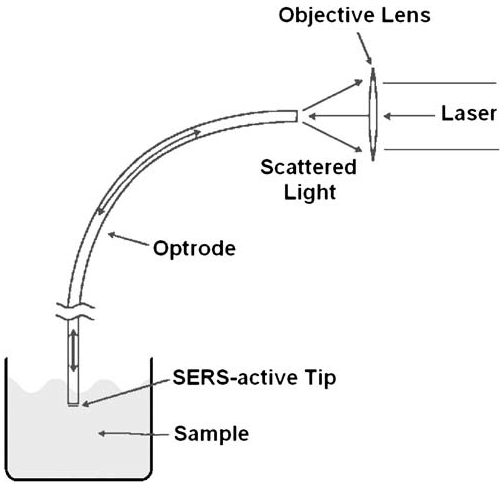

Figure 1.4 Schematic of SERS optical fiber probe.[14]

Single-ended measurement geometry requires SERS nanostructure coupled on fiber facet to be reasonably transparent so that Raman scattered light can be collected by the fiber and

transmitted to the spectrometer. The most commonly used SERS substrate to couple with optical fiber is Ag or Au nanoparticles (NPs). [13, 29-31] These nanoparticles can be attached on fiber facet through *in situ* synthesis or using APTMS sol–gel as linker between nanoparticles and silica surface. Nanoparticles coated optical fiber probe for *in situ* SERS measurement [30, 31] can achieve SERS EF on the order of 10^4-10^5, lower than the common single molecule SERS EF of ~10^7-10^8 [1]. In general, combination SERS platform with optical fiber is challenging but promising for *in vivo* biosensing. Many researches regarding sensitivity and stability of SERS optrode remain to be accomplished to develop a better understanding of SERS optrode performance.

1.5 Outline of the Thesis

Chapter 2 describes the experimental and theoretical studies of an optical fiber probe with nanostructured end-facet for biosensing applications *via* SERS. Factors affecting Raman signal intensity through the fiber probe are investigated. Raman signal loss through fiber compared with optical microscope based free-space Raman detection is estimated. To further enhance the SERS enhancement factor, a hybrid graphene/Au nanotriangle structure is transferred on the end-facet of the fiber probe to enable SERS.

Chapter 3 presents an investigation of theoretical simulation featuring three-dimensional finite difference time domain (FDTD). Excitation of SPPs by circular Au rings and coupling of SPPs with Au pyramids are studied to improve the electric field and the overall SERS enhancement of the platform. Structural variables that could affect the coupling efficiency

between SPPs and LSP are investigated systematically to obtain optimal design. The study aims at finding the quasi-quantitative relation between several key-variables of the pyramid-ring combination and the overall SERS enhancement at the center of the structure. The incorporation of the LSP−SPP hybrid structure onto the facet of optical fiber for SERS-based detection is also investigated.

Chapter 4 describes the study on a practical way of patterning metallic nanostructures for achieving high SERS enhancement factors (EFs) and high hot spot density. By simply superimposing one Au triangle array on another to form multilayer triangle array, SERS signal can be enhanced by two orders of magnitude compared with one layer triangle array. FDTD simulation and a mathematical model are employed to study how the number of layers affects the SERS enhancement. The simulation results indicate that the drastic increased SERS EFs and hot spot density are due to an increase of amount of gaps formed between Au triangles and a decrease of the gap size.

Chapter 5 presents the exploration of the feasibility of combining other vdW materials (MoS_2) with plasmonic surface for SERS detection. Enhanced light–matter interactions in bilayer MoS_2-covered gold nanopyramids are investigated. Prominent resonance Raman and photoluminescence spectroscopic differences between AA' and AB stacked bilayer MoS_2 grown by chemical vapor deposition are studied. Both resonance Raman and photoluminescence spectra show distinct features indicating clear differences in interlayer interaction between these two

phases.

Chapter 6 concludes the thesis by providing the major results with a section that proposes future work that can build on the results presented herein.

Chapter 2 SERS Optical Fiber Probe with Plasmonic End-facet

2.1 Introduction

In vivo biosensing is tremendously needed for health care and biomedical researches. For example, an estimated 5.4 million Americans are living with Alzheimer's disease (AD)[32], an irreversible, progressive brain disorder which can slowly destroys memory and thinking skills. However, the cause of AD is still poorly understood. Plaques comprised of Amyloid-b (Ab) peptide appears in the brain of AD patients, but the link between Ab peptide and the cause of AD is still needed to be verified [33, 34]. *In vivo* detection of the Ab with high sensitivity and quantitative analysis is thus highly demanded for understanding of pathology and diagnostics of Alzheimer's disease. *In vivo* neurochemical measurement is one of the key approaches to investigate neuron communication as well as brain function, but still remains a great challenge considering the low concentration of neurotransmitters (tens of nanomolar)[35], small release region, and rapid concentration change[36]. All these features of neurochemical processes require the biosensor to have high sensitivity, high spatial resolution and temporal resolution. In addition, it is often desirable for biosensing involving animal subjects to allow animal movement in order to observe behavior during the measurement, which requires the measurements to be compatible with animal movement. Therefore, typical requirements for biosensor used in *in vivo* biosensing include reasonable sensitivity and specificity for analytes, quantitative analysis, and appropriate spatial and temporal resolution.

Raman is a spectroscopy technique that can provide characteristic spectral information of anlaytes although the yield of Raman scattering is very low leading to weak Raman signals in most cases. Surface enhanced Raman spectroscopy (SERS) makes up this deficiency *via* plasmon resonance. It is capable of ultra-sensitive detection (single molecule detection) and allows for label-free detection with high degree of specificity[1]. Molecules absorbed at nanostructured metallic surface experience a large amplification of electromagnetic field due to local surface plasmon resonance leading to orders of magnitude increase in Raman yield and greatly enhanced Raman signal. To achieve high SERS enhancement factors, many efforts have been devoted to develop various metallic (mainly Au and Ag) nanostructures to enhance the local electromagnetic field [7, 9, 10]. In addition to traditional metallic nanostructures, graphene and other 2-dimentional materials have also been explored to enhance Raman signal [5, 37-39]. SERS has been explored for *in vivo* tumor detection with labeled Au nanoparticles [26, 40], in which the specificity of detection is enabled by labeling technique. Compared with labeled nanoparticles, SERS optical fiber probe with single ended measurement geometry[16, 17] has been gaining attention for *in vivo* label-free biosensing due to their flexibility and compatibility with remote sensing. A label-free detection scheme allows real-time detection and eliminates time and cost consuming labeling procedures[28]. Moreover, label-free SERS renders vibrational information akin to finger-prints of bio-molecules that is in principle more specific than any labeling approaches. The most common method to couple SERS substrates with optical fiber is to modify

the fiber end with SERS substrates such as Ag or Au nanoparticles (NPs) [13, 29-31]. Nanoparticles coated optical fiber probe for *in vitro* SERS measurement [30, 31] can achieve enhancement factor on the order of 10^4-10^5, lower than common single molecule SERS EF of ~10^7-10^8 [1]. SERS fiber probes prepared using this method have spatial resolution similar to fiber core diameter (usually larger than 10 μm). However, higher spatial resolution is demanded in certain biosensing, like *in vivo* neurochemical monitoring [41]. For instance, measurement of neurodynamics within individual synaptic clefts (tens of nanometers[42]) represents the most extreme challenge. To expand the SERS fiber probe for *in vivo* biosensing, optimization of SERS fiber probe is required to provide higher SERS EF and spatial resolution.

The optimization of SERS fiber probe can be achieved only if key factors affecting sensitivity are well understood. This chapter describes our effort in gaining such understanding. In this study, we prepare SERS fiber probes based on Au nanotriangle array and propose a method to enhance the spatial resolution of SERS fiber probe. The key factors studied here include numerical aperture (N.A.) of objective lens, slit width of spectrometer, fiber length and size of SERS nano-array. Raman signal loss through the fiber is estimated compared with normal Raman detection. To further enhance SERS EF, a hybrid graphene/Au nanotriangle structure is transferred on fiber facet. SERS fiber probe with hybrid graphene/Au nanotriangle structure is found to have better performance than the fiber probe with bare Au nanotriangle structure.

2.2 Experimental

2.2.1 Fabrication of SERS Optical Fiber Probe

The SERS fiber probe is prepared by transferring Au nanotriangle array onto the fiber facet. The optical fiber (Thorlab FG050LGA) used has a 50 μm core diameter and its N.A. is 0.22. Figure 2.1 shows the fabrication process. SiO_2 (50 nm)/Si substrate is first patterned with Au square (80 nm thickness) with an opening window using normal photolithography. Polystyrene (PS) nanospheres (500nm diameter) are coated on patterned SiO_2/Si substrate through dip-coating method. 120 nm Au film is deposited on the PS/SiO_2/Si sample by E-beam evaporation, after which the whole sample is ultrasonicated in ethanol for 3 min to lift off PS spheres. The as-prepared sample is then washed by deionized water for 3 times.

Au nanotriangle array is transferred on fiber facet with the assistance of polymethyl methacrylate (PMMA) layer. PMMA is first coated on the SiO_2/Si substrate with Au triangle array. Then the sample is put onto the surface of HF or KOH solution to etch the SiO_2 layer in between PMMA and Si substrate. Once the SiO_2 is completely etched, PMMA layer with Au nanotriangle array and patterned Au film will flow on the surface of the etching solution. Next the PMMA film is washed by deionized water and transferred onto the fiber facet. Micromanipulator is used to align the Au nanotriangle array right on the fiber core. After the sample dried, oxygen plasma is used to remove the PMMA layer covered on Au nanotriangle array. In this way, only the Raman signal generated by Au nanotriangle array within the opening

window region can pass through the fiber to the spectrometer. Raman signal generated elsewhere is blocked by the 80 nm Au film, which will absorb ~99.7% of the Raman light. By changing the window size in Au square pattern, spatial resolution of the fiber probe can be tuned.

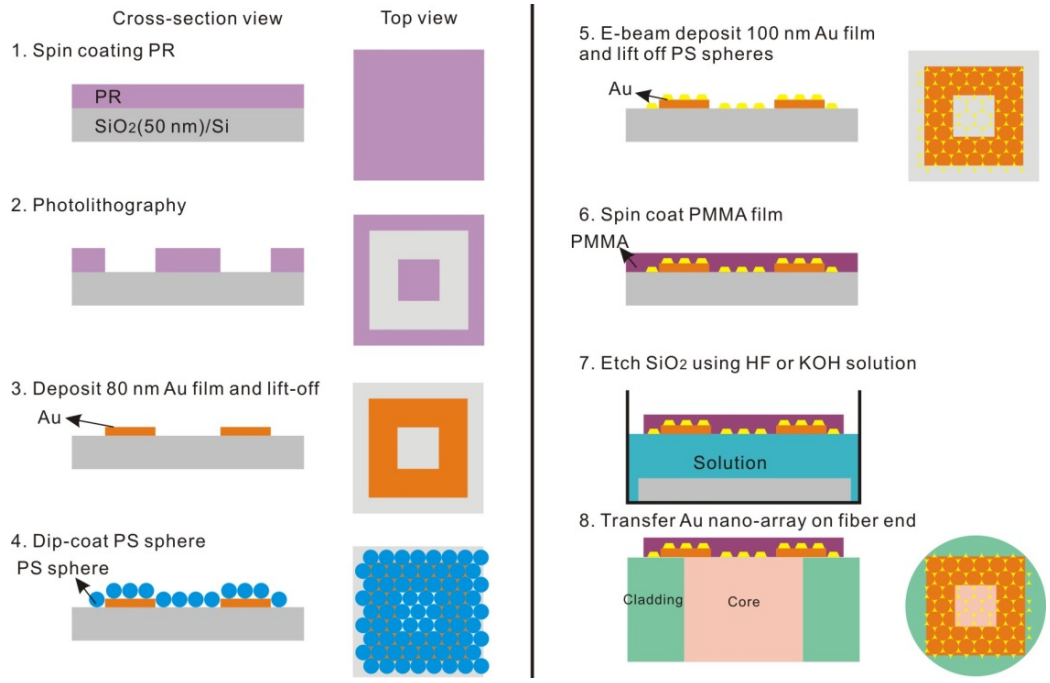

Figure 2.1 Schematic of fabrication process of SERS fiber probe.

2.2.2 Growth and Transfer of Graphene

Graphene used in the experiment is grown by CVD method using copper foil. [43] 25 micron-thick copper foil (Alfa Aesar #13382) is cut into a 2×2 inch square. The copper foil is loaded onto the center of a quartz chemical vapor deposition (CVD) chamber, the furnace is heated up to ~1025°C under the flow of H_2 (~1000 sccm). After 30 minute annealing, the CVD growth is carried out with 20 Torr total pressure with CH_4 (~20 sccm) and H_2 (~1000 sccm) for 15 minutes. Then the chamber is cooled down to room temperature.

A thin layer of PMMA is uniformly spin coated on the synthesized graphene sample. The metal catalyst Cu is removed in an etching solution combined $CuCl_2$ (2.5 M) and HCl (37 wt%) aqueous solution with volume ratio of 4:1. Then the floating PMMA-graphene structure is transferred onto the surface of de-ionized water. Subsequently the sample is transferred onto the fiber facet with Au nanotriangle array using the similar method describe above, but the PMMA layer covering graphene is removed by acetone followed by isopropanol alcohol and deionized water washing.

2.2.3 SERS Measurement Setup

SERS measurement is conducted using Renishaw inVia confocal Raman microscope with 785 nm laser (12.5 mW power with 20 s accumulation time). The SERS optical fiber is coupled to microscope using a home-made fiber holder. Figure 2.2 (a) shows the schematic diagram of the experiment setup. R6G is used as analyte molecule in this study. Unless otherwise stated, the R6G Raman data are obtained in liquid solution in the following experiment. SEM image in Figure 2.2 (b) shows the Au nanotriangle array transferred on the fiber end.

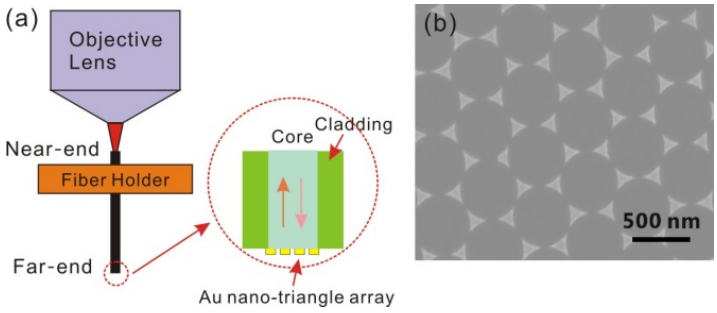

Figure 2.2 (a) Schematic diagram of the experiment setup. (b) SEM image of Au nanotriangle array.

2.3 Results and Discussion

2.3.1 Effect of Numerical Aperture of Objective Lens on Raman Signal

We first consider the effect of N.A. of objective lens on Raman signal. Figure 2.3 (a) shows the Raman spectra measured from the same SERS fiber probe with different objective lens. The slit width of the spectrometer is chosen as 300μm for all three lenses to make sure all the Raman scattered light coming out of near end of fiber can be collected by spectrometer. The highest Raman signal intensity is achieved by 20× lens with 0.4 N.A., followed by 50× lens with 0.75 N.A. Five characteristic Raman peaks of R6G, 1311, 1360, 1507 1595 and 1648 cm^{-1} can be distinguished clearly using 20× lens. Raman signal obtained from 50× lens has lower intensity than that from 20× lens but the R6G peaks are still discernible. However, Raman spectrum obtained from 5× lens does not show any discernible R6G peaks. For a given SERS fiber probe with analyte molecules on its far end, Raman signal intensity (S) obtained through the fiber can be expressed as follows:

$$S \propto I_0 \cdot a \cdot b$$

Where I_0 is incident laser power on the near end of fiber, a is the coefficient representing the percentage of laser power that coupled into the fiber, and b is another coefficient representing the percentage of Raman signal coming out of the fiber (near end) that collected by the objective lens. The precondition for this expression is that laser focused spot size is smaller than that of fiber core. For 5×, 20×, and 50× lens, the R6G 1360 cm^{-1} peak intensity as seen in Figure 2.3 (a)

are about 0, 10000 and 2000 counts, respectively. This can be reconciled with the expected values based on the consideration that $(a \cdot b) = (0.22/NA_{lens})^2$. The calculated value (0.302) for 20× lens is about 4 times of that value (0.085) for 50× lens, which is in reasonable agreement with the experimental result. The only noticeable difference is for 5× lens, which could be explained by that the laser focused spot size for 5× lens is larger than the fiber core, and therefore laser power coupled into fiber also decreases (a <1). The combination of the two factors (a<1 and $b=(0.22/NA_{lens})^2$) causes the Raman signal intensity with 5× lens the lowest. Based on the above discussion, higher Raman signal can be achieved when the N.A. of the objective lens close to or match the N.A. of the fiber, assuming other conditions are the same.

2.3.2 Effect of Slit Width of Spectrometer on Raman Signal

Next factor affecting Raman signal is the slit width of spectrometer. Raman signal intensity dependence on slit width is shown in Figure 2.3 (b), where R6G 1360 cm^{-1} peak intensity is used as a metric of Raman signal intensity. By increasing the slit width from 50 to 400 μm, Raman signal increases by ~200% for 20× lens while background noise increases by ~20%. Thus widening the slit actually improves the signal to noise ratio (S/N). The trend continues up until the slit width reaches 250 μm for 20× lens. The reason is that beyond that value the signal stops increase with noise continues going up, making the 250 μm width the optimum for S/N. This optimum value is dependent on N.A. of the lens and it is 400 μm for 50× lens. This can be understood as follows. When the Raman signal from the near end of the fiber comes into the

objective lens and is collected by the spectrometer, the image of fiber core is projected on the slit of spectrometer, as shown in Figure 2.3 (c). If the magnified fiber core image size is larger than the slit width, part of the Raman signal does not enter into the spectrometer. When the magnified fiber image just matches the slit width, the Raman signal intensity reaches the maximum. Further increasing the slit width will not help enhance the signal intensity but increase the stray light and cause noise. For 20× lens, Raman signal saturates at 250 μm slit width, which means the core image is enlarged for about 5 times at slit width. The magnification for 50× lens is larger than 20×, so the enlarged fiber core image on the slit is also larger, and thus the signal should saturate at larger slit width. Therefore, by increasing the slit width within certain range, Raman signal intensity can be enhanced. In the following Raman measurement, 20× lens and 300 μm slit width are used.

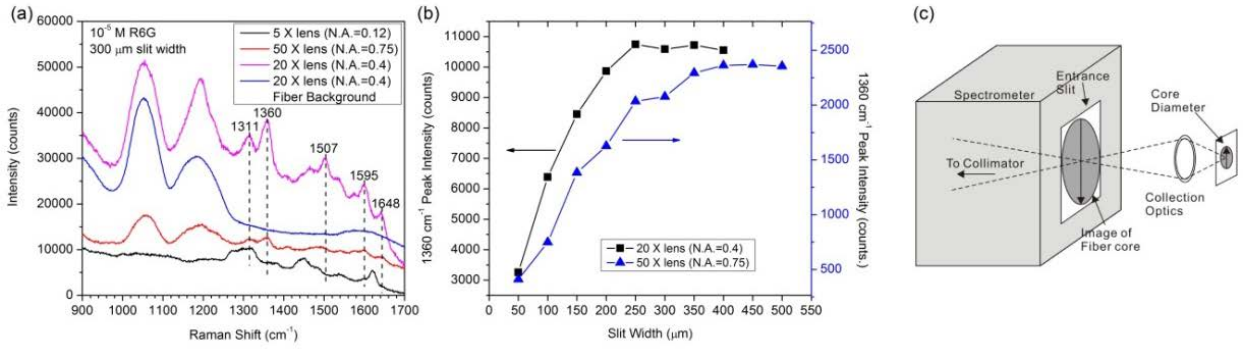

Figure 2.3 (a) Raman spectra of R6G measured with SERS fiber probe (11 cm long) using different lens, (b) Dependence of R6G peak intensity on spectrometer slit width, (c) Illustration of fiber-to-spectrometer matching.[44]

2.3.3 Effect of Fiber Length on Raman Signal

To study how fiber length affects Raman signal intensity, we investigated the S/N of R6G Raman peak and the noise dependence on fiber length. R6G 1360 cm^{-1} peak is chosen to calculate the S/N. As shown in Figure 2.4 (a), the S/N changes from about 5 for 400 cm long fiber to about 11 for 3 cm long fiber, increasing by about 2 times. The noise changes from about 2000 counts for 400 cm long fiber to about 800 counts for 3 cm long fiber, decreasing by about 2 times. Figure 2.4 (b) shows the Raman spectra of R6G measured using SERS fiber with different length. As the fiber length increases, the florescence background of fiber keeps increasing. Figure 2.4 (c) indicates the bare fiber background intensity (1053 cm^{-1} broad peak) dependence on fiber length, which shows a linear relationship between background intensity and fiber length within the length scale investigated. It is worth noting that in Figure 2.4 (b) the R6G Raman peak intensity keeps constant as fiber length increases to 400 cm. This observation is consistent with the theoretical calculation based on the fiber attenuation. The attenuation of the fiber used is about 8 db/km in the range of 750-800 nm, which means the Raman signal loss within the fiber is negligible (<0.5%) for fiber less than 5 m. The above analyses indicate that the increase of the noise mainly comes from the fiber background as fiber length increases, which causes the decrease of the S/N ratio. Therefore, the fiber length is not a primary concern for Raman signal intensity loss within the length scale investigated here, but it will affect the S/N of the Raman spectrum and thus affect the performance of SERS fiber probe. The impact on S/N from the fiber

fluorescent background can be partially reduced by increasing the collection time or using long wavelength laser.

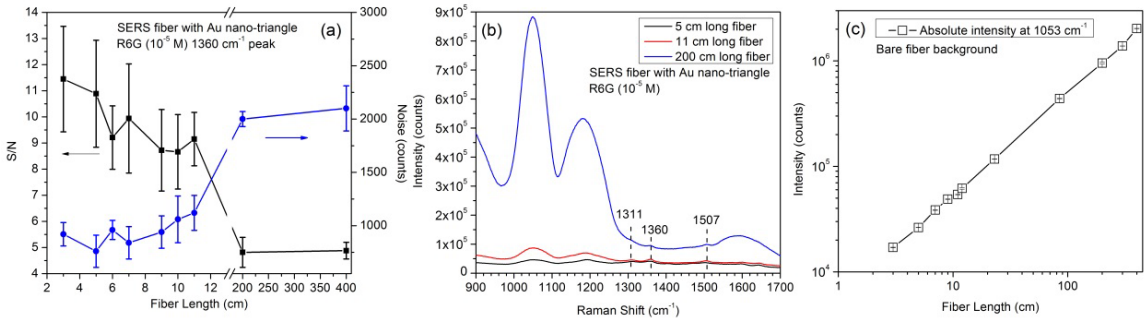

Figure 2.4 (a) S/N ratio and noise dependence on SERS fiber length. (b) Raman spectra of R6G measured using SERS fiber probe with different length (Background of fiber was not removed). (c) Fiber background intensity dependence on fiber length.

2.3.4 Effect of Nanoarray Size on Raman Signal and Raman Signal Loss Estimation

As seen in Figure 2.5(a), Raman signal intensity increases with SERS array area on fiber end (Figures 2.5(b-d)). For SERS fiber with Au-triangle array coated on the whole fiber core (50 μm diameter), highest Raman signal can be achieved and the detection limit can reach 10^{-6} M for R6G solution. As SERS array decreases to a 10 μm-length square, no R6G Raman peak is discernible. The Raman signal increases linearly with SERS array area and the spatial resolution is proportional to the square root of the area. Our results indicate that there is a fundamental tradeoff between spatial resolution and signal intensity. Spatial resolution improves with smaller surface area, provided the signal is still detectable. To achieve higher spatial resolution of the SERS fiber probe, higher SERS EF of the nanostructure is required to compensate for the

decrease of the SERS array size.

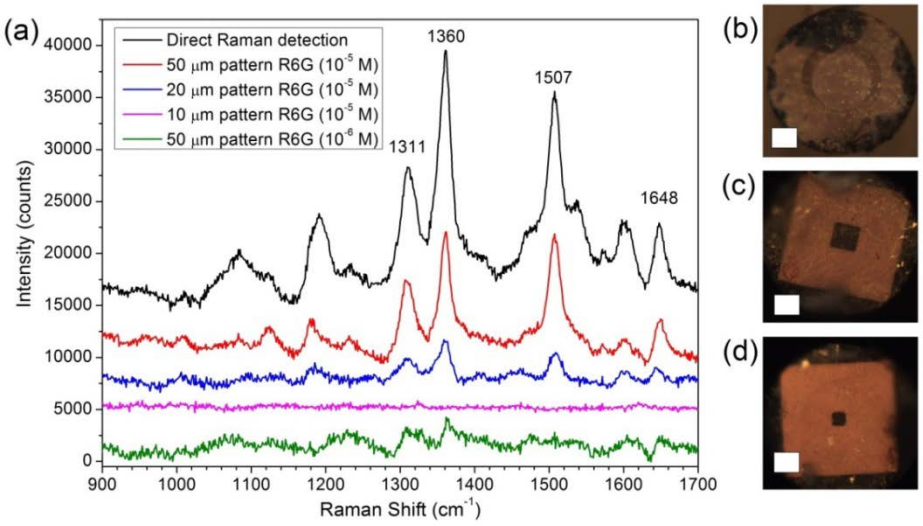

Figure 2.5 (a) R6G Raman spectra obtained by SERS fiber probes (11 cm long). Fiber background has been removed in (a). For comparison, R6G spectrum (black curve) measured by the free-space detection scheme (Raman signal directly enter into objective lens) is also shown in (a). (b-d) Optical image of fiber probe with Au triangle array covering the whole surface (b), 20 μm Au array (c) and 10 μm (d) Au array covering on fiber core. Scale bar in (b), (c) and (d) are 20 μm.

To estimate the Raman signal loss of the SERS fiber probe compared with direct Raman detection method, Raman measurement of R6G (10^{-5}M) on Au nanotriangle array is conducted. For direct Raman detection, laser is directly focused on the fiber end with SERS substrates, and the Raman signal is collected by objective lens. SERS fiber probe used for direct Raman detection is first immersed into R6G solution (10^{-5} M) for 10 minutes, and then dries for measurement. Black spectrum in Figure 2.5 (a) shows the R6G Raman spectrum measured through the direct detection. Taking R6G 1360 cm^{-1} peak intensity as a metric, Raman signal

intensity measured by the direct method is about 2 times of that measured through fiber probe, indicating the Raman signal loss due to fiber is about 50%. When experimental setup is fixed, Raman signal intensity can be expressed as follows,

$$S \propto \frac{I_0}{A} A_D D \Omega t$$

where S is Raman signal intensity expressed in Raman photons, I_0 is incident laser power (photons·s^{-1}) shinning on the analyte molecules, A is laser spot area (cm^2), A_D is the sample area monitored by spectrometer (cm^2), D is the molecule density(#·cm^{-2}), Ω is the solid angle collected by objective lens (sr), and *t* is collection time (s). In SERS fiber probe detection method, laser light comes out from 20× objective lens (N.A.=0.4) and couples into the fiber (N.A.=0.22), in which only 30.25 % of laser intensity (I_0) is coupled into the fiber and finally illuminates molecules on the fiber core. For direct Raman detection, laser spot area (A) is the same as the sample area (A_D) monitored by spectrometer. For the fiber detection, the spectrometer slit width has been enlarged so that the entire fiber core image can entrance the slit, which also means A is equal to A_D. The molecule density D and collection time *t* are the same for both detection methods. Raman signal coming from laser spot region is collected by 20× lens (N.A.=0.4) for the direct detection, but for the fiber detection Raman signal coming from fiber core region (N.A.=0.22) is collected by objective lens. Due to the smaller N.A. of fiber, the solid angle value for the fiber detection is only 30.25% of that for the direct detection. Based on the above analysis, the Raman signal measured by fiber method is approximately 10% (30.25%×30.25%) of that

measured by the direct detection, which is comparable with the experimental results (about 50% loss). It is worth noting that laser power density (photos·s^{-1}·cm^{-2}) at molecules decreases for fiber detection method compared with direct Raman detection, but the larger fiber core area (i.e. larger amount of analyte molecules) compensates for the laser power density decrease. Therefore, to keep the spatial resolution (laser focused spot size is about 4 μm for 20× lens) of direct Raman detection, we need to reduce the SERS nanoarray size on fiber facet to the similar size of laser spots. In this situation, laser power density decrease will became the primary factor which contributes to the Raman signal loss. Therefore, SERS nanostructure with higher EF is required to compensate for the laser power density decrease.

2.3.5 Graphene/Au Hybrid SERS Fiber Probe

To improve EFs of SERS fiber probes, graphene is transferred on Au nanotriangle array on SERS fiber probe (Inset image in Figure 2.6(a)). Through superimposing graphene over metallic SERS substrates, higher SERS enhancement factor has been obtained for selected families of molecules.[5] In our experiment, we do observe this enhancement using graphene/Au hybrid SERS fiber probe, as seen in Figure 2.6(a). Graphene 2D and G peak are readily apparent and graphene D peak overlaps with R6G 1311 cm^{-1} peak. R6G Raman peak intensities measured by Au/graphene fiber probe are larger than that by the fiber probe with bare Au nano-array for the same concentration of R6G solution (10^{-6} M), which is due to the chemical enhancement of graphene. The introducing of graphene not only enhanced the Raman signal intensity but also

would help *in vivo* biosensing using SERS fiber probe due to its bio-compatibility and chemical-stability.[45-47] Through transferring graphene/Au hybrid substrates on fiber, we have demonstrated that Au triangle/ graphene are suitable for fiber-based SERS sensing applications. Although the SERS enhancement for this hybrid SERS substrate is relatively low compared to nanoparticle-based substrates, the substrate has larger SERS-active zones than nanoparticle-based substrates. As shown in the FDTD simulated electric field distribution (Figure 2.6 (b)), the enhanced electric field extends 50 nm into the gaps between Au nano triangles, much larger than the gap formed in nanoparticle-based substrates. Such large SERS-active zone makes this structure suitable for label-free direct SERS sensing of macromolecules such as proteins and DNAs. In addition, the properties of graphene make it possible to modulate SERS effects using the hybrid graphene/metallic nanostructures.

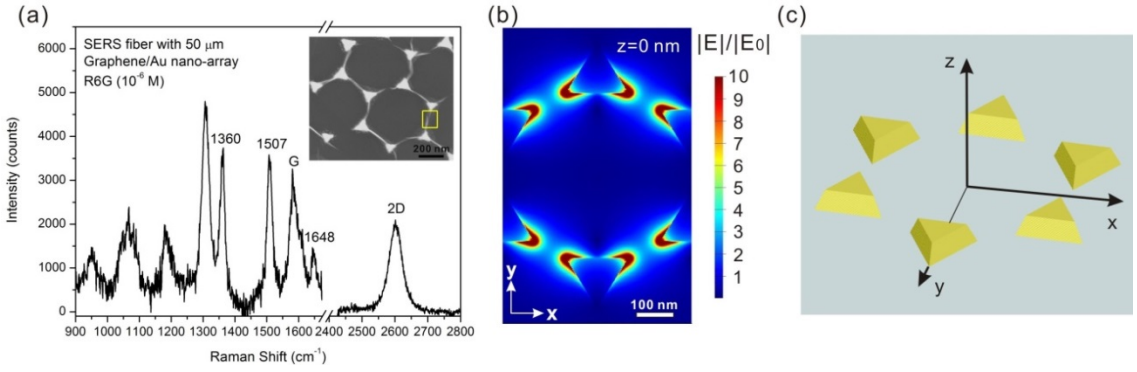

Figure 2.6 (a) R6G Raman spectrum obtained by SERS fiber probe with graphene/Au nanotriangle (11 cm long). Inset SEM image shows graphene covering on Au nanotriangle. Yellow boxed area indicates the graphene fold formed between neighboring Au triangles. (b) Electrical field magnitude mapping along x-y plan for z=0 nm. (c) Schematic model of Au triangle array used for FDTD simulation, in which

incident light is along z axis and polarization direction is along *x*-axis.

2.4 Conclusion

In conclusion, Au nanotriangle array based SERS fiber probe is prepared. Effects of optical lens, slit width, fiber length and array size on Raman signal intensity are investigated. Matching N.A. of lens to N.A. of fiber and matching of slit width to size of enlarged fiber core image can help increasing Raman signal. Raman signal intensity appears to be independent of fiber length up to several meters but S/N will decrease with fiber length. Size of SERS array coated on fiber facet is one primary factor accounting for the Raman signal loss, which is ultimately due to laser power density decrease on the fiber end. SERS fiber probe with hybrid graphene/Au nano-array is found to be superior to the fiber probe with bare Au nano-array in terms of the sensitivity. The fabrication method proposed here can be used to further enhance fiber probe spatial resolution.

Chapter 3 Coupling SPP with LSPR for Enhanced Field Confinement: A FDTD Simulation Study

3.1 Introduction

The electromagnetic (EM) enhancement is the major mechanism for SERS enhancement, in which local EM field is enhanced due to the excitation of localized surface plasmon (LSP) of metal nanostructures. This enhancement of EM field accounts for the increase of the Raman signal intensity of adsorbates on (typically) metallic surfaces. In addition to LSP, surface plasmon polaritons (SPPs) are another potential source of EM enhancement. It has been shown that metallic ring structure can focus SPPs into its geometric center and create an intense spot of near field optical intensity on a flat metal surface.[48-52] However, Raman enhancement factor (EF) due to the focused SPPs by ring structure is low compared with LSP.[53] Coupling between SPP and LSPR on nanohole/nanocone arrays has also been explored to enhanced the local electrical field recently, and shown improved Raman detection performance.[54]

To achieve strong Raman signal, high local EM field is required in SERS metallic nanostructures. Tremendous efforts have been spent on engineering the structure of metal nanostructures to obtain high local EM field.[18-22] Among these nanostructures, nanogap formed between metal nanoparticles (NPs) is a highly effective SERS nanostructure, which can boost the Raman signal up to ~10^9 times.[21] The deficiency of this kind of structure is the small detection volume, typically below 10 nm. With such small size of detection volume, it is difficult for large

molecules like proteins to fit in the gap where the hot spots are located. Compared with nanogap between adjacent NPs, nanopyramid array is an open structure, in which hot spots locate between neighboring pyramids.[5, 6] As such, large molecules can easily move into these regions and their Raman signals can be enhanced. The shortcoming of nanopyramid arrays is that the magnitude of EM field at the hot spots is not as high as that in NPs. This chapter discusses the use of SPP lunched by circular ring structure combined with the LSP generated near nanopyramids to enhance local EM field.

We systematically investigate structural variables that could affect the coupling efficiency between SPP and LSP to obtain optimal design using finite-difference time domain (FDTD) simulation. This study aims at finding the quasi-quantitative relation between several key-variables as detailed below of the pyramid-ring combination and the overall SERS enhancement at the center of the structure. Such highly localized (within ~10 nm range) and extremely intense (as high as 10^4 times the intensity of a tightly focused laser beam) non-propagating electric field has many potential applications including biosensing, surgery, and biomedical research. The structural variables affecting the focus of SPPs are adjusted systematically to optimizing performance. We consider the following factors that could affect the interaction between SPP and LSP, ring radius, number of rings, pyramid spacing, number of pyramids, and the relative position of ring center and pyramid array center. The SERS performance of different structures is evaluated based on integral of $|E|^4$ value over space. We also

carry out the study of the LSP-SPP hybrid structure on the tip of optical fiber probes with the intended application for *in vivo* biosensing (Section 3.3.4)

3.1.1 Surface Plasmon Polariton (SPP)

A plasmon is a quantum quasi-particle, which represents the elementary excitations of the charge density ossilation in a plasma. Polaritons describe the coupled state between an elementary excitation and a photon. When light interacts with metal, the optical response of a metal in the visiable and infrared is dominated by the interaction of light with free-electron plasma. The EM waves in a metal are called plasmon-polaritons. Surface plasmon is a kind of plasma modes in thin film, corresponding to longitudinal charge density waves propagating at metal/dielectric surface. SPP corresponds to a mixed mode where the energy is shared between the charge density wave (surface plasmon) and the EM wave (photon). SPP modes on a planar metal surface are bound to the metal surface and guided by it, propagating until their energy is lost either to absorption in the metal or scattering into other directions (such as into free space).

As is stated above, SPP is a kind of EM wave propagating along the surface of interface. SPP modes can be described by the surface plasmon–polariton dispersion relation, the relationship between the angular frequency (ω) and in-plane wavevector (k) of SPP modes. Next, we will give a brief derivation of the surface plasmon–polariton dispersion relationship and the SPP wavelength. Let us consider EM wave propergating along an interface between a metal film with dielectric constant ε_m and a dielectric film with dielectric constant ε_d.(Figure 3.1)

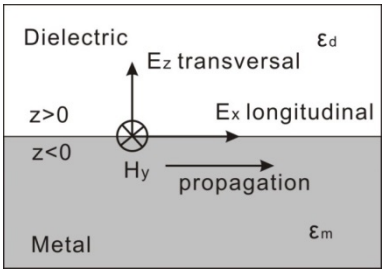

Figure 3.1 Schematic figure of propagating SPPs with transversal E_z and longitudinal E_x and H_y.

Planar wave on the surface can be written in Equation (3.1) and (3.2):

$$H(x,y,z,t) = (H_x, H_y, H_z)\, exp\big[i\big(k_x x + k_y y + k_z z - \omega t\big)\big] \tag{3.1}$$

$$E(x,y,z,t) = (E_x, E_y, E_z)\, exp\big[i\big(k_x x + k_y y + k_z z - \omega t\big)\big] \tag{3.2}$$

SPP is a transverse magnetic (TM-polarized) wave, and thus we can get

$$E_x, E_z \; and \; H_y \neq 0 \tag{3.3}$$

$$E_y = H_x = H_z = 0 \tag{3.4}$$

By plugging (3.3) and (3.4) into (3.1) and (3.2), we can get

$$\boldsymbol{H}_d = (0, H_{yd}, 0)\, exp[i(k_{xd}x + k_{zd}z - \omega t)] \tag{3.5}$$

$$\boldsymbol{E}_d = (E_{xd}, 0, E_{zd})\, exp[i(k_{xd}x + k_{zd}z - \omega t)] \tag{3.6}$$

$$\boldsymbol{H}_m = (0, H_{ym}, 0)\, exp[i(k_{xm}x - k_{zm}z - \omega t)] \tag{3.7}$$

$$\boldsymbol{E}_m = (E_{xm}, 0, E_{zm})\, exp[i(k_{xm}x - k_{zm}z - \omega t)] \tag{3.8}$$

From Maxwell equation $\nabla \times \mathrm{H} = \varepsilon \frac{\partial \mathrm{E}}{\partial \mathrm{t}}$, we can get

$$\begin{pmatrix} -\partial_z H_y \\ 0 \\ \partial_x H_y \end{pmatrix} = -\frac{\varepsilon\omega}{c} \begin{pmatrix} E_x \\ 0 \\ E_z \end{pmatrix} \tag{3.9}$$

For dielectric, we have

$$k_{zd} H_{yd} = +\varepsilon_d \frac{\omega}{c} E_{xd} \tag{3.10}$$

$$k_{xd} H_{yd} = -\varepsilon_d \frac{\omega}{c} E_{zd} \tag{3.11}$$

For Metal, we have

$$k_{zm}H_{ym} = -\varepsilon_m \frac{\omega}{c} E_{xm} \tag{3.12}$$

$$k_{xm}H_{ym} = -\varepsilon_m \frac{\omega}{c} E_{zm} \tag{3.13}$$

At the interface boundary, we have

$$H_{yd} = H_{ym}, E_{xd} = E_{xm}, E_{zd} = E_{zm} \tag{3.14}$$

Therefore,

$$\frac{k_{zd}}{\varepsilon_d} + \frac{k_{zm}}{\varepsilon_m} = 0 \tag{3.15}$$

On the other hand, we have

$$k_x{}^2 + k_z{}^2 = k^2 = \frac{\varepsilon\omega^2}{c^2} \tag{3.16}$$

At the interface, we can get

$$k_{xd} = k_{xm} = k_x \tag{3.17}$$

For dielectric:

$$k_x{}^2 + k_{zd}{}^2 = \frac{\varepsilon_d\omega^2}{c^2} \tag{3.18}$$

For metal:

$$k_x{}^2 + k_{zm}{}^2 = \frac{\varepsilon_m\omega^2}{c^2} \tag{3.19}$$

As a result, from Equation (3.15), (3.18) and (3.19), we can get

$$k_x{}^2 = \frac{\omega^2}{c^2}\frac{\varepsilon_m\varepsilon_d}{\varepsilon_m + \varepsilon_d},\ k_{zd}{}^2 = \frac{\omega^2}{c^2}\frac{\varepsilon_d{}^2}{\varepsilon_m + \varepsilon_d},\ k_{zm}{}^2 = \frac{\omega^2}{c^2}\frac{\varepsilon_m{}^2}{\varepsilon_m + \varepsilon_d} \tag{3.20}$$

Therefore, we obtain the surface plasmon–polariton dispersion relationship shown in below.

$$k_x = \frac{\omega}{c}\sqrt{\frac{\varepsilon_d\varepsilon_m}{\varepsilon_d + \varepsilon_m}} = k_x{}' + ik_x{}'' \tag{3.21}$$

From the above dispersion relationship, we can get the SPP wavelength, i.e. the period of

the surface charge density oscillation and associated field distribution of the mode. The SPP wavelength can be obtained from the complex dispersion relation by taking the real and imaginary parts respectively. The real part (k_x') of the surface plasmon wavevector k_x is

$$k_x' = \frac{\omega}{c}\sqrt{\frac{\varepsilon_d \varepsilon_m'}{\varepsilon_d + \varepsilon_m'}} \tag{3.22}$$

Where ε_m' is the real part of the metal dielectric constant. From this the SPP wavelegnth, λ_{spp}, is given by $\lambda_{spp} = 2\pi/k_x'$.

$$\lambda_{spp} = \lambda_0\sqrt{\frac{\varepsilon_d + \varepsilon_m'}{\varepsilon_d \varepsilon_m'}} \tag{3.23}$$

where λ_0 is the free space wavelength.

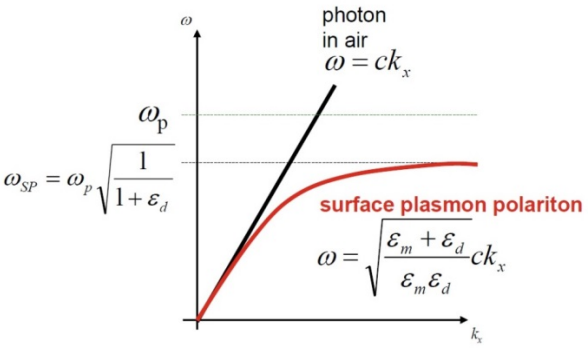

Figure 3.2 Dispersion relation of SPPs.

As seen from the SPP dispersion relations (Figure 3.2), the SPP wavevector is larger than the photon wavevector in the adjacent dielectric medium; thus, light illuminating a smooth surface cannot be directly coupled to surface polaritons. To meet the requirement of wavevector conservation, special experimental arrangements have been designed. One way of matching the photon and SPP wavevectors is to use total internal reflection geometry or Kretschmann and Otto

configurations (Figure 3.3). In the Kretschmann configuration (Figure 3.3a), the metal film is illuminated through the dielectric prism at an angle of incidence greater than the angle of total internal reflection. The wavevector of light is increased in the optically dense medium. At a certain angle of incidence θ where the in-plane component of the photon wavevector in the prism coincides with the SPP wavevector on an air–metal surface, the parallel momentum $\hbar k_x = n_p \hbar k_0 sin\theta$ (n_p is the refractive index of prism) in the prism is then transferred by the evanescent field through the metal and can excite SPP modes of the metal/dielectric interface. In addition, coupling SPPs to light can be achieved through relaxing the conservation of momentum restriction, i.e. break the translational invariance. This can be achieved by engraving a periodic structure on the surface along the x direction (Figure 3.3e), or generating a random surface roughness (Figure 3.3f). Besides that SPPs can also be excited by scanning near-field optical microscopy (SNOM) probe. [55]

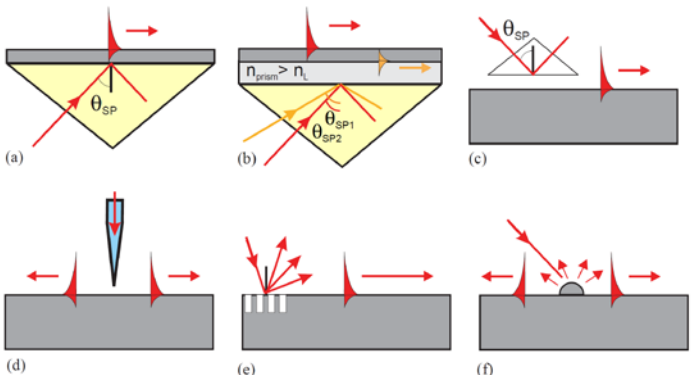

Figure 3.3 SPP excitation configurations: (a) Kretschmann geometry, (b) two-layer Kretschmann geometry, (c) Otto geometry, (d) excitation with an SNOM probe, (e) diffraction on a grating, and (f) diffraction on surface features. [55]

3.1.2 Finite Difference Time Domain (FDTD) Method

The three dimensional finite difference time domain method (FDTD) is widely used in nanoplasmonic simulations. FDTD is a powerful numerical tool for theoretical studies of the SERS EM enhancement mechanism, and a useful tool for the design of SERS substrate with higher sensitivities and spectral spatial resolution. In the FDTD approach, both space and time are divided into discrete segments. Space is segmented into box-shaped "cells" with the electric fields located on the edges of the box and the magnetic fields positioned on the faces, as shown in Figure 3.4. This orientation of the fields is known as the "Yee cell" or "Yee grid". In FDTD method, time is quantized into small steps where each step represents the time required for the field to travel from one cell to the next.

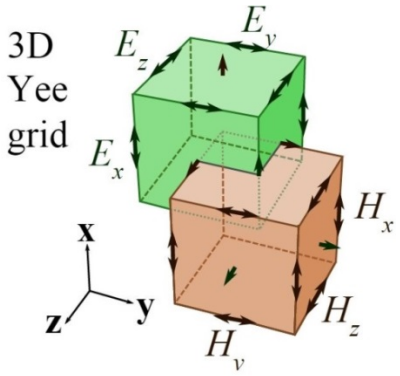

Figure 3.4 Illustration of a standard Cartesian Yee cell used for FDTD[56].

The basic principle of FDTD is to numerically solve Maxwell's differential equations

$$\nabla \times \boldsymbol{E} = -\frac{\partial \boldsymbol{B}}{\partial t} \tag{3.24}$$

$$\nabla \times \boldsymbol{H} = \boldsymbol{J} + \frac{\partial \boldsymbol{D}}{\partial t} \tag{3.25}$$

where ***E***, ***D***, ***H***, ***B***, ***J*** represent the electric field, electric displacement, magnetic field, magnetic induction intensity and current density, respectively.

Taking that function *f(x,y,z,t)* denotes the electric or magnetic field in the coordinate system, we have the form $f(x,y,z,t)=f(i\Delta x,j\Delta y,k\Delta z,n\Delta t)=f^n(i,j,k)$.Then *f(x,y,z,t)* can be discretized via the central difference approximation in both space and time:

$$\left.\frac{\partial f(x,y,z,t)}{\partial x}\right|_{x=i\Delta x} \approx \frac{f^n\left(i+\frac{1}{2},j,k\right)-f^n\left(i-\frac{1}{2},j,k\right)}{\Delta x} \tag{3.26}$$

$$\left.\frac{\partial f(x,y,z,t)}{\partial y}\right|_{y=j\Delta y} \approx \frac{f^n\left(i,j+\frac{1}{2},k\right)-f^n\left(i,j-\frac{1}{2},k\right)}{\Delta y} \tag{3.27}$$

$$\left.\frac{\partial f(x,y,z,t)}{\partial z}\right|_{z=k\Delta z} \approx \frac{f^n\left(i,j,k+\frac{1}{2}\right)-f^n\left(i,j,k-\frac{1}{2}\right)}{\Delta z} \tag{3.28}$$

$$\left.\frac{\partial f(x,y,z,t)}{\partial t}\right|_{t=n\Delta t} \approx \frac{f^{n+\frac{1}{2}}(i,j,k)-f^{n-\frac{1}{2}}(i,j,k)}{\Delta t} \tag{3.29}$$

By solving these discrete equations using numerical methods, electric and magnetic fields associated with each Yee cell can be obtained. The Yee cell size can affect the accuracy of the calculated field distribution. Typically, Yee cell size should be significantly smaller than the smallest excitation wavelength, and smaller Yee cell size will generate more accurate calculation results. However, due to the limitation of computation resources, cell size cannot be infinitely small. To save computational time, non-uniform Yee cell method is also developed.

3.2 FDTD Simulation Model Setup

Concentric rings of Au are employed for launching SPPs. An Au pyramid array is placed at

the center of the rings to generate LSP. The magnitude of electric field of Au pyramid array is calculated using FDTD method (Lumerical FDTD Solutions). The calculations are set up as a three-dimensional system with a 4 nm resolution cubic grid, and including the appropriate boundary conditions. The excitation light is modeled as a normal incident plane wave of 633 nm wavelength, considering that 633 nm laser is one of the most commonly achievable lasers. The polarization of light is along *x*-axis. The direction of the incident light is set to illuminate the pyramid array from the top side onto the apex of the pyramids (along –*z*-axis) for simulation in section 3.3.1 to 3.3.3, and from the bottom side onto the bases of the pyramids (along +*z* direction) for section 3.3.4.

The amplitude of electric field of incident light ($|E_0|$) is set to be 1. The calculated amplitude of electric field ($|E|$) appears as the ratio of $|E|/|E_0|$. The absolute amplitude of electric field of the incident light is determined by the incident laser power. For example, a beam of 633 nm laser with 5 mW power and 1 μm-diameter laser spot will generate a light intensity of 6.36×10^5 W/cm^2, and the corresponding value of $|E_0|$ is 0.022 MV/cm. The local electric field enhancements depend strongly on the exact position of the SERS substrate surface. Thus, the SERS EFs on the surface of a typical SERS substrate are highly non-uniform, even at a molecular scale of nanometers. For detection of trace amount of molecules, both hot spots and their size need to be considered for the evaluation of the overall enhancement of SERS substrates. The metrics we use for quantify SERS performance consists a combination of high electric field and large volume

with sufficiently high electric field. We choose 10 as a threshold value of |E| for SERS hot spots. In other words, when the value of |E| within one mesh box is large than 10, we consider that mesh box as a SERS hot spot. To quantitatively characterize the overall SERS enhancement of each pyramid-ring combination, we apply an integral of $|E|^4$ value over space based on the common $|E|^4$-approximation.[17] More specifically, we calculate the sum of $|E|^4$ value of every hot spot ($\sum_{|E|\geq 10} |E|^4$) within a fixed space (640×640×160 nm). So obtained is the overall enhancement value used to evaluate the performance of various Au nanostructures in the following discussion.

3.3 Results and Discussion

3.3.1 Electric Field Distribution of a 4-Pyramids Array

A 4-pyramids array pattern is chosen as the basic structure. Figure 3.5(b) shows the schematic diagram of the pyramid model. Each pyramid has a 200 nm base length and 140 nm height. The continuous Au film beneath the pyramids is 20 nm thick. Figure 3.5(a) shows the 2-dimentional (2D) electric field distribution of the 4-pyramids array along *x*-*y*, *x*-*z*, and *y*-*z* plane. Hot spots are mainly located on the ridge and the apex region of the pyramids and the volume of hot spots is small compared to the Au pyramid structure. The total volume of hot spots only accounts for less than 0.5% of the volume of one Au pyramid and the maximum $|E|/|E_0|$ value at hot spots is 12. The simulation results indicate that Au pyramid array alone cannot render high electric field together with large detection volume. Therefore, improvement of both hot spots number and electric field at

hot spots around pyramid array are needed for highly sensitive detection of trace amount molecules.

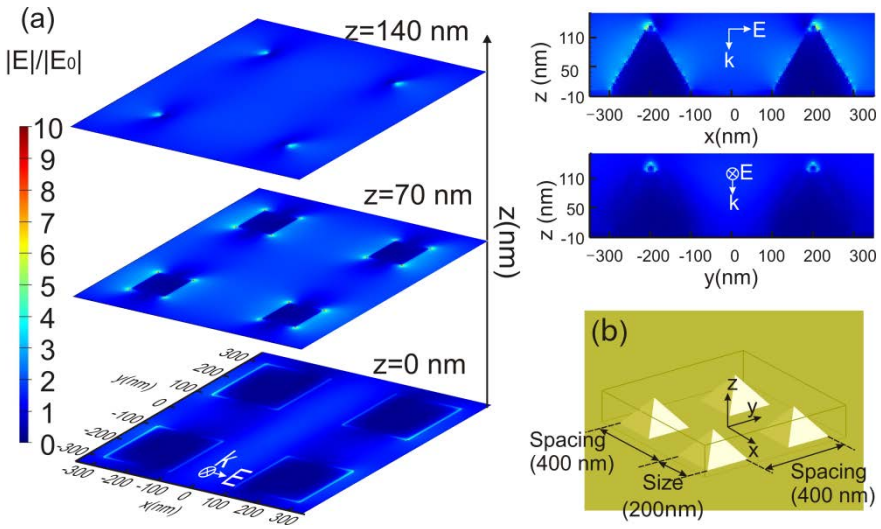

Figure 3.5 (a) The 2D electric field distribution of 4-pyramids array along *x*-*y*, *x*-*z* and *y*-*z* plane (excitation wavelength=633 nm); (b) Schematic diagram of the 4-pyramids array used for simulation.

3.3.2 Enhancement of Electric Field by Focusing SPPs to a 4-Pyramids Array

Circular metallic rings are known to possess the ability of launching and focusing SPPs into its center.[51, 52] By placing the pyramid array in the center of the metallic circular ring, it is possible to enhance the electric field of Au pyramids further. In this section, we will discuss the structural variables directly influencing the electric field of Au pyramids. These variables include the radius of the rings, and the number of rings.

3.3.2.1 Effect of Ring Radius on Electric Field

A circular ring is designed to excite SPPs and focus them into the center. Figure 3.6(a) shows the schematic diagram of Au ring and its cross-section view. The height of the ring is 60 nm and

the width of the ring is 200 nm. For 633 nm light excitation, SPP wavelength (λ_{spp})[57] on Au is 598.2 nm and propagation length (δ_{spp})[57] of the SPP is 8 μm, which is about 13 times of the SPP wavelength. Plasmon focusing with linearly polarized light usually results in an inhomogeneous plasmon focal spot owing to the symmetry mismatch between incident polarization and plasmonic structures.[52] Figure 3.6(b) shows the 2D electric field distribution at the center of bare Au ring structure with radius of 22 λ_{spp}. A minimum electric field is created at the geometric focus, which is due to the destructive interference between counter-propagating surface plasmon waves. This inhomogeneous plasmon focal spot can be viewed as two SPP focal spots, at which $|E|/|E_0|$ value is about 3, apparently lower than the $|E|/|E_0|$ value of hot spots of the 4-Au pyramids array (Figure 3.5(a)).

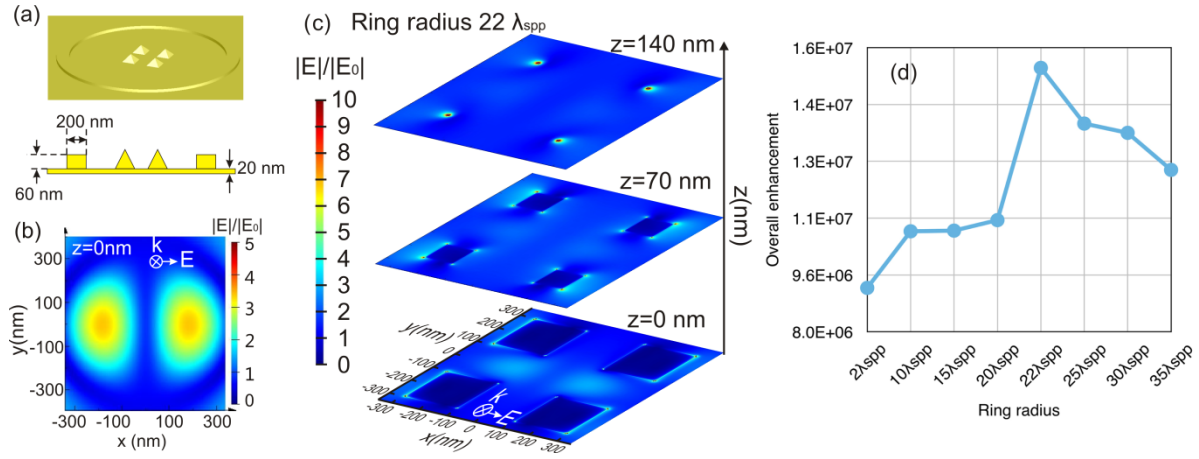

Figure 3.6 (a) Schematic diagram of Au pyramid array located at the center of the ring and its cross-section view. (b) 2D electric field distribution at the center of single Au ring (R=22λ_{spp}). (c) 2D electric field distribution of 4-pyramids array after adding one Au ring (R=22λ_{spp}). (d) Overall SERS enhancement with increasing radius of the ring (excitation wavelength=633 nm).

By placing the 4-pyramids array at the center of the ring, focused SPPs are able to couple with the LSP generated by pyramid structure, leading to stronger electric field around pyramids. We then consider the effect of ring radius (R) on the overall SERS enhancement. The radiuses of the rings range from 2 λ_{spp} to 35 λ_{spp}. Figure 3.6(c) shows the 2D electric field distribution of Au pyramid array after adding one Au ring ($R=22\lambda_{spp}$). Figure 3.6(d) shows the dependence of the overall SERS enhancement of Au pyramids-ring structures on the ring radius. As the ring radius increases from 2 to 35 λ_{spp}, the overall enhancement of Au pyramids-ring first increases and then decreases with maximum value at the radius of about 22 λ_{spp}. Compared with bare Au pyramids array, Au pyramids array with ring structure enhances both the number of hot spots and the maximum $|E|/|E_0|$ value at hot spots.

For bare metallic ring, the intensity of electric field at the center first increases and then decreases as the radius of the ring is increased.[52] This trend of the intensity is determined by two competing processes, increased source of SPPs and enhanced intensity loss due to SPP damping. Assuming each small segment of the ring as an SPP generator, total electric field generated by the whole ring should be in proportion to its radius R. Meanwhile, the field intensity also decays as $\exp(-R/\delta_{spp})$. Thus the SPP intensity in the center of the ring should be proportional to $R\exp(-R/\delta_{spp})$. We can easily obtain a "first increasing then decreasing" trend with a critical point at $R=\delta_{spp}$. After combining Au pyramids array with Au ring, a similar trend is observed on our structure, but the focused SPPs start to couple with LSP generated by Au pyramid structure, which should make

the dependence relation more complicated. That is probably why our maximum overall enhancement is found at about $22\lambda_{spp} \approx 1.6\delta_{spp}$ rather than δ_{spp}. Table 3.1 shows the contribution of the various site enhancements to the total SERS enhancement (here defined as $\sum_{|E|\geq 1} |E|^4$) for Au pyramid array with one ring ($R=22\lambda_{spp}$). The hottest sites ($|E|/|E_0|>10$) contain just 0.03% of all the mesh boxes (within 640×640×160 nm region) but contribute 35% of the total SERS enhancement, illustrating the reason why we define 10 as a threshold value of $|E|/|E_0|$ for SERS hot spots.

Table 3.1 Contribution of various site enhancements to the total SERS enhancement ($R=22\lambda_{spp}$)

$\|E\|/\|E_0\|$	Percentage of mesh boxes	Percentage of contribution to the total enhancement
1-5	99.76%	43%
5-10	0.21%	22%
10-16	0.03%	35%

3.3.2.2 Effect of the Number of Rings on Electric Field

In this section, we increase the number of rings to enhance the excitation of SPPs. For multiple concentric rings structure, if the locations of the additional rings satisfy the circular Bragg condition for plasmonic wavelength, the electric intensity of the plasmonic focus will get stronger while the focal spot remains approximately the same size as more rings are added. In the following simulation, the number of rings is increased from 1 to 18. We start from the largest ring with a radius of 20 λ_{spp}, and each new ring is added with one λ_{spp} smaller radius. For the 18th ring, radius is $3\lambda_{spp}$. Figure 3.7(a) shows the 2D electric field distribution along *x*-*y* planes for Au pyramids

with 15 rings added. The electric field between pyramids and the hot spot volume are strongly enhanced compared with the situation without rings (Figure 3.5(a)). The increased rings contribute to the dramatically enhanced excitation of SPPs, which mainly account for the enhancement of electric field near pyramids. Figure 3.7(b) shows the overall SERS enhancement with increasing number of the rings. The overall enhancement of substrate first gradually improves as more rings are added, but starts to decrease as ring number further increases to 18. As the ring number increases, SPP sources increase, but scattering due to the presence of inner ring will also increase. These two competing mechanism determines the amount of SPPs which could be coupled into the central pyramid array. As the number of rings increases to certain amount, scattering starts to dominate and we see that the overall enhancement decrease as the number of rings is increased.

Figure 3.7(c) shows the calculated extinction, absorption and scattering curve of the 4-pyramids array with 15 rings, and the wavelength dependence of its overall SERS enhancement. The extinction curve does not show an apparent resonance peak, but the overall enhancement shows a clear maximum value near 610 nm. At the wavelength smaller than 575 nm, the enhancement of electric field near Au pyramid is very small with no electric field amplitude ($|E|/|E_0|$) being larger than 10. The discrepancy between extinction curve and overall enhancement dependence on wavelength can be understood from the following two aspects. First, the distance between neighboring Au rings is set as one plasmonic wavelength based on the 633 nm excitation. When excitation wavelength is far away from 633 nm, the plasmonic wavelength will change

correspondingly, and thus the neighboring rings will no longer satisfy the circular Bragg condition for the plasmonic wavelength. As such, SPP wave is not constructively interferenced, and the amount of SPPs focused to the center of ring will decrease dramatically, leading to the low enhancement of electric field. Second, scattering starts to dominate the extinction for longer wavelength despite the reduction in plasmon resonance related absorption, as seen in Figure 3.7(c). In addition, the enhancement of local electrical field around pyramids are mainly due to the coupling between SPP and LSP. Extinction curve can reflect the LSPR frequency but probably not appropriate to characterize the optimum frequency for the coupling between SPP and LSP. In the following simulation, we will continue to use 633 nm wavelength for excitation of SPP and LSP.

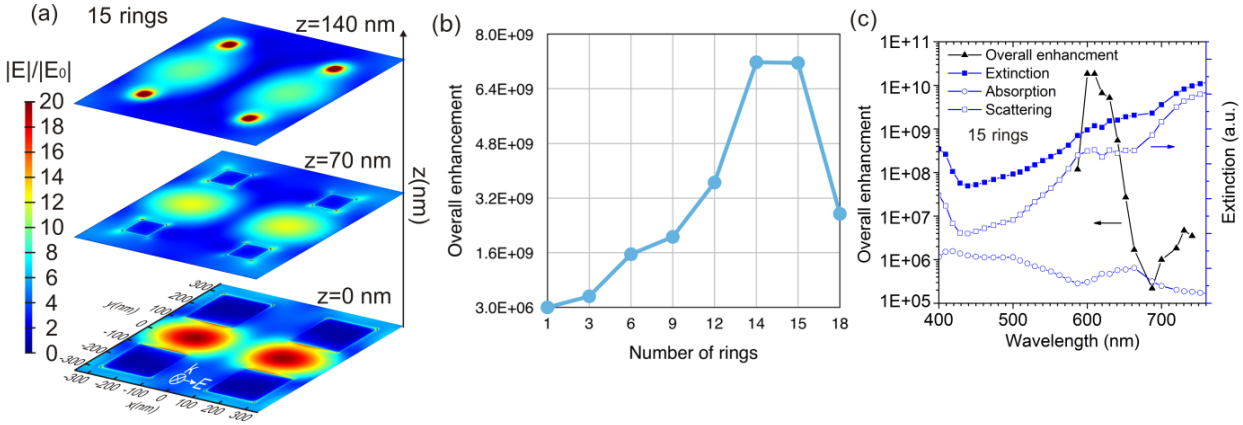

Figure 3.7 (a) The 2D electric field distribution of 4-pyramids array (with 15 rings) along *x*-*y* plane; (b) Overall enhancement with increasing number of the rings (excitation wavelength=633 nm). (c) Extinction absorption and scattering curve of Au pyramid array with 15 rings, and the overall enhancement change with excitation wavelength.

3.3.3 Coupling Efficiency of SPPs and 4-Pyramids Array

In this section, the coupling efficiency of the focused SPPs and pyramid array is discussed. The structural variables could affect the coupling efficiency are investigated, including the pyramid spacing, the distance of pyramid array center to the ring center, and the number of pyramids. We assume that the structural variables affecting the LSP and SPP interaction do not have an obviously convoluted effects with one another. In other words, the change of one structural variable will not influence the way that another variable affects the LSP and SPP coupling. Based on the assumption, the number of rings is fixed to be 6 with smallest ring size of 15 λ_{spp} and the largest ring size of 20 λ_{spp} for simulation in section 3.3 and 3.4 in order to save the computational resource.

3.3.3.1 Simulation of Varying Spacing between the Pyramids

In this section, the spacing (S) between neighboring pyramids varies from 200 nm to 600 nm to couple with SPPs. Figure 3.8 shows the 2D electric field distribution and overall SERS enhancement for varying spacing between pyramids. The pyramids with 250 nm spacing generate larger hot spot volume than pyramids with 500 nm spacing (Figure 3.8(a,b)). When the spacing is increased from 200 to 600 nm, the general trend of overall enhancement is first increasing and then decreasing. This can be understood from the relative position between Au pyramids and SPP focal spots. The Au rings focus SPPs into its center to form two SPP focal spots (Figure 3.8(b)). The more the Au pyramids overlap with SPP focal spots, the stronger the coupling between SPP and

LSP. Therefore, pyramids overlap with the SPP focal spots the most will lead to the highest overall SERS enhancement.

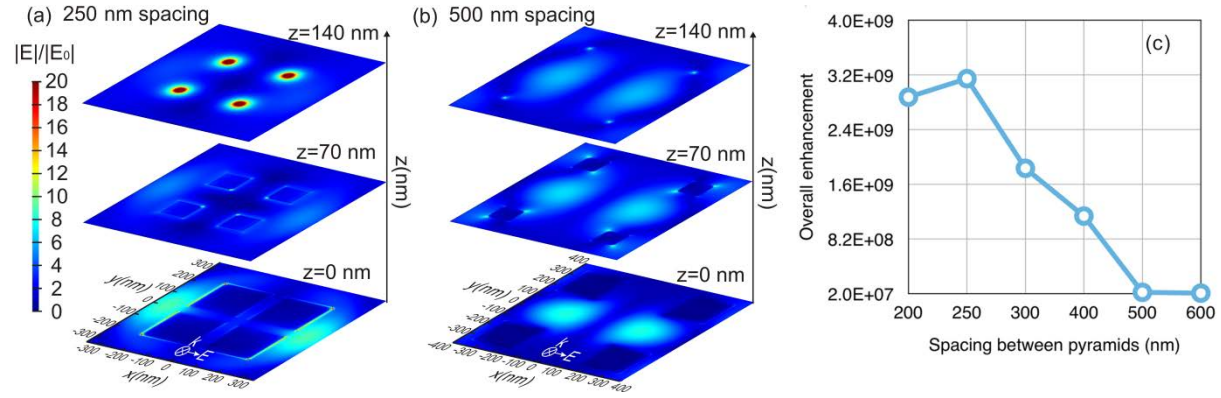

Figure 3.8 The 2D electric distribution of pyramids array with different spacing between pyramids: (a) 250 nm (b) 500 nm. Mappings in (a) and (b) have the same scale bar for $|E|/|E_0|$. (c) Overall enhancement with increasing spacing between pyramids (excitation wavelength=633 nm).

3.3.3.4 Simulation of Varying Distance of Pyramid Array Center to the Ring Center

In this section, the position of 4-pyramids array is shifted from the ring center to study the coupling efficiency of LSP and SPPs. The distance (D) of the pyramid array center to the ring center varies from 0 nm to 600 nm along *x*-axis. Figure 3.9 shows the 2D electric field distribution and overall SERS enhancement with various distances. SPPs are focused into the center of the ring pattern, and thus the general trend is that the further the pyramid array away from the ring center, the less efficient they are coupled and thus the weaker enhancement. However, when the pyramids are moved away from the ring center, it will encounter the peaks and troughs of SPPs along the way, which will lead to fluctuation of coupling efficiency and thus the fluctuation of overall enhancement, as seen in Figure 3.9(c).

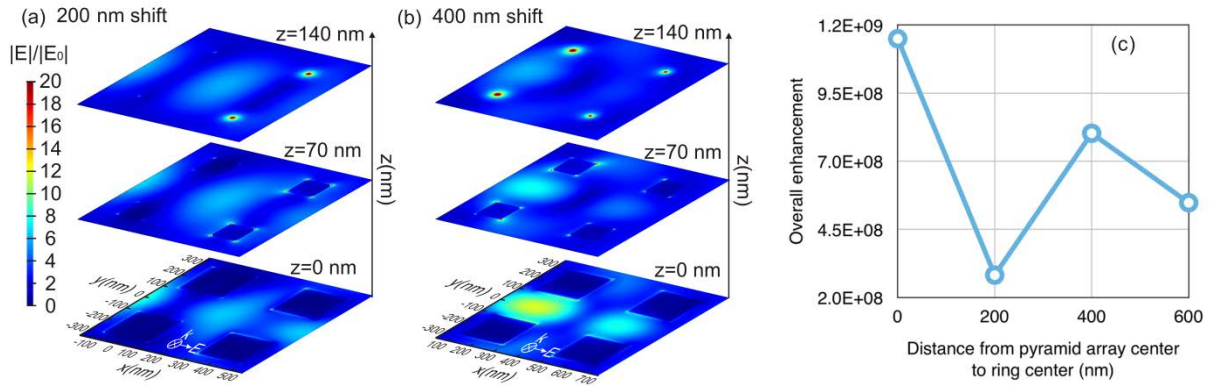

Figure 3.9 The *x-y* plane 2D electric field distribution of increasing distance between pyramids center to the ring center: (a) 200 nm (b) 400 nm. Mappings in (a) and (b) have the same scale bar for $|E|/|E_0|$. (c) Overall enhancement with increasing distance between pyramids center to ring center (excitation wavelength=633 nm).

3.3.3.5 Simulation of Varying Number of Pyramids

In this section, one, two and three pyramids are taken away from the 4 pyramids pattern. The positions of the left three, two and one pyramid are chosen to overlap most part of the hot spot region generated by SPPs. Figure 3.10 shows the 2D electric field distribution of different pyramid pattern and the overall enhancement with increasing number of pyramids. When the number of pyramids becomes smaller than 4, the enhancement can actually be stronger. The underlying mechanism is that a pyramid stand right on the SPP focal spot can provide the strongest enhancement, as is mentioned in section 3.3.3.1. For the 4-pyramids array, SPP focal spots only appear in the gaps between pyramids (Figure 3.5 (a)), while the one, two and three pyramids array all have at least one pyramid standing right on the SPP focal spot. Not only would the results give us a hint of how to couple LSP and SPP efficiently, it also suggests that by reducing pyramid number, the electric field can be further confined spatially without sacrifice of the electric field

intensity.

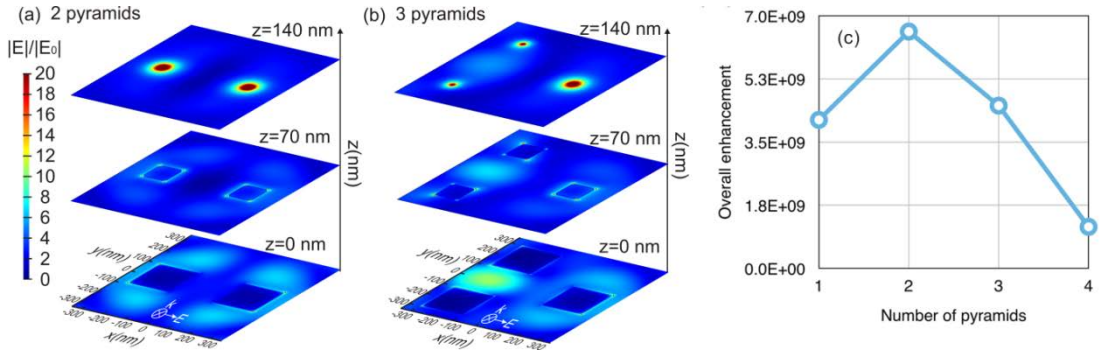

Figure 3.10 The *x-y* plane 2D electric field distribution for different number of pyramids: (a) 2 pyramids and (b) 3 pyramids. Mappings in (a) and (b) have the same scale bar for $|E|/|E_0|$. (c) Overall enhancement with increasing number of pyramid (excitation wavelength=633 nm).

3.3.4 Fiber-Based Probe with Back Illumination and Signal Extraction

One objective of this simulation is to guide the fabrication of SERS optical fiber probe for remote sensing. The fabrication process requires transferring the 4-pyramids pattern onto the optical fiber end, where the incident light is illuminating from the backside (bottom) of the pyramids. In this case, signal extraction could be difficult for certain reasons. One of the main issues is that Au film substrate will absorb the signal while it travels through. Two approaches can be employed to address this issue, one is to reduce the thickness of continuous film, the other is to open a window in the continuous film to let light pass through. The following simulations is to determine the signal extraction efficiency in the case of fiber-based probe with back illumination

In this simulation, the thickness of Au continuous film beneath rings is adjusted from 20 nm to 0 nm. When the thickness of the film changes from 20 nm to 0 nm, the enhancement of electric

field increases dramatically. Figure 3.11(a) shows the 2D electric field distribution of 0 nm Au film. Because substrate without a continuous film will reduce the chance that the incident light and Raman signal absorbed by Au film, and thus has a higher signal extraction efficiency. For comparison, pyramids without ring structure are also simulated, whose performance is shown in Figure 3.11 (c). Again, it can be seen that by adding ring structure, the enhancement increases significantly, indicating effective coupling between SPP and LSP. Another way of increasing the signal extraction efficiency is to remove part of the continuous Au film substrate, as show in the inset of Figure 3.11(c). 2D electric field distribution of broken film is shown in Figure 3.11(b). Compared with 20 nm continuous film, broken film generates higher enhancement, which is yet lower than that with 0 nm film thickness.

The common single-ended SERS fiber probe is prepared by coating metallic NPs or transferring nano-patterns on the facet of one optical fiber.[29-31] Because the Raman signal come back to spectrometer through the same fiber core, SERS fiber probes prepared using this method detects signal from across the entire fiber facet (usually larger than 10 μm) rendering the SERS spatial resolution on the same order of magnitude. With the pyramid-ring structure, on the other hand, the excitation EM field energy is concentrated to the array of pyramids, which could cover orders of magnitude smaller area compared to the area of the fiber facet. Because SERS yield is proportional to the fourth power of the amplitude of the EM field, this concentration of the EM field leads to drastically improved spatial resolution. Our simulation results indicate that the Au

pyramid-ring can confine the electric field within a 700×700 nm region. The pyramid-ring structure could provide higher spatial resolution for SERS optical fiber probe than those of the previously reported SERS fiber probes if the pyramids-ring SERS platform were transferred onto the optical fiber facet.

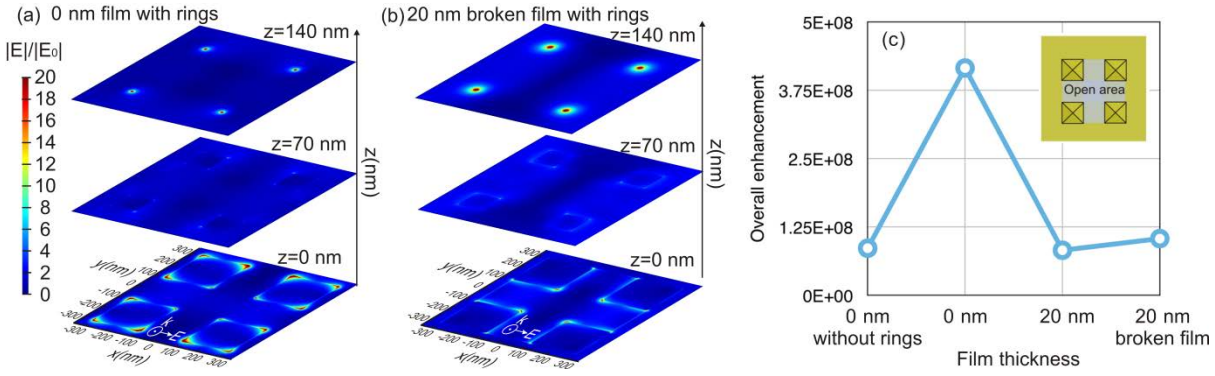

Figure 3.11 The 2D electric field distribution for different thickness of Au films: (a) 0 nm (b) 20 nm with opening window between pyramids. (c) Overall enhancement with increasing substrate thickness from back illumination (excitation wavelength=633 nm). Inset shows the schematic diagram of non-continuous Au film substrate.

3.4 Conclusion

This research demonstrates a novel open-structured Au pyramids SERS platform with enhancement of the spatial confinement of the electric field. Excitation of SPPs by circular Au rings and coupling of SPPs with Au pyramids are studied to improve the electric field and the overall SERS enhancement of the platform. By combination of Au pyramids with Au rings, the hot spot volume as well as electric filed intensity at hot spots around Au pyramid are increased

significantly compared with bare Au pyramids array. We also find out that the more pyramid overlaps with the SPP focal centers, the higher coupling efficiency can be achieved, therefore leading to more hot spots and higher electric field enhancement. By changing the number of pyramids and their positions, the electric field enhancement up to 140× can be achieved and the anticipated SERS signal enhancement of up to 8 orders of magnitude. The results of simulation with back light illumination demonstrate that the thickness of Au film substrates plays a significant role for the signal extracting from backside when the SERS platform are transferred onto a fiber facet. Highest electric field enhancement can be achieved without the Au film for fiber application. Au pyramids combined with rings could achieve the confinement of the electric field within a 700×700 nm region, which could provide higher spatial resolution for SERS fiber probe.

Chapter 4 Multilayer Metallic Nanostructures for Strong SERS Enhancement

4.1 Introduction

SERS technique has been widely used for trace amount detection of molecules due to its high sensitivity.[5-8] To detect molecules with ultra-low concentrations, especially single molecule SERS (SM-SERS) detection, hot spot (sites with high electric field on plasmonic surfaces) distribution plays an important role. It is well known that a small fraction of the sites on SERS substrates contribute to the majority of the Raman signal.[58] For SM-SERS, randomly absorbed molecules have to overlap in position with one of the hot spots on plasmonic surfaces. To obtain as much statistics as possible on ultra-low concentration detection events, not only the electrical field at hot spots but also the hot spot density needs to be high.

Many efforts have been devoted to develop various metallic (mainly Au and Ag) nanostructures to enhance the local electromagnetic field.[18-22, 59] Among these plasmonic surface fabrication methods, nanostructure prepared by nanosphere lithography[60-63] is a relatively convenient and low cost method to prepare SERS substrates with periodical nanopattern. Ag and Au nanotriangle array made using this method show high SERS EFs. The hot spots of triangle array are mainly located near gaps between neighboring triangles or sharp corner of triangles. However, single layer triangle array only accounts for about 12% of the total area of the substrate surface, which means there is still room to enhance the hot spot density.

In this chapter, we study on a practical way of patterning metallic nanostructures for achieving high SERS EFs and high hot spot density for detection of biological entities. This method produces metallic nanostructures of nearly triangular shape. Our results indicate that by simply superimposing one layer Au triangle array on another to form multiple layered (hereafter multilayer) triangle array, SERS signal can be enhanced by two orders of magnitude compared with monolayer Au triangle array. The local electrical field enhancement of multilayer Au triangle array is also investigated by FDTD and theoretical simulation. The easy method proposed here expands the application of nanosphere lithography technique.

4.2 Experimental

4.2.1 Micro-Raman Spectra and Mapping

Raman spectra are measured using a Renishaw inVia microscope under 633 nm laser excitation. The laser power used is 1 mW. The grating used is 1800 l/mm, and the objective lens used is 50× (NA 0.75). A step size of 2 μm is used for Raman mapping. Raman data are analyzed using Renishaw WiRE 4.0 software. The collection time for each spectrum is 1 s.

To reflect SERS enhancement of the entire surface of the multiple layered Au triangle array, we conducted 3 Raman mappings with more than 400 spots on the entire surface of each kind of samples. The Raman mapping data obtained are used to do the statistical analysis.

4.2.2 Fabrication of multilayer Au triangle array

Monolayer Au nanotriangle array is fabricated by nanosphere lithography using 500 nm diameter polystyrene nanospheres. Multilayer Au nanotriangle array is prepared by transferring monolayer nanotriangle array on another using PMMA as a sacrificial support layer.

Figure 4.1 shows the schematic of fabrication process of multilayer Au nanotriangle array. Monolayer Au nanotriangle array is prepared using nano sphere-lithography.[60] Multilayer Au triangle array is prepared through superimpose one layer Au triangle array on another. Step 1 is to coat polystyrene (PS) spheres (500 nm in diameter) on SiO_2/Si substrates to form hexagonal close packed pattern. Typical size of PS spheres for SERS substrate application is around several hundreds of nanometers. Step 2 is to deposit 120 nm thick Au film on the PS spheres using electron-beam deposition. Step 3 is to lift off the PS spheres. The prepared sample from Step 2 is soaked into acetone and ultra-sonicated for at least 10 min to remove the PS spheres. Step 4 is to spin coat PMMA layer on Au triangle/SiO_2/Si substrates. The speed for coating is 2000 rpm and the time is 20s. Step 5 is to detach the PMMA/Au triangle film from the SiO_2/Si substrate by placing the sample prepared in Step 4 onto the surface of KOH solution (~30wt%). After several minutes, the thin SiO_2 layer will be etched away by KOH and the PMMA/Au triangle film will floated on the surface of KOH aqueous solution. Then PMMA/Au triangle film is transferred on DI water using a dummy Si wafer to clean the film. Step 6 is to transfer the PMMA/Au triangle film on another Au triangle layer (sample in Step 4) using simple scope technique. After the

PMMA/Au triangle film fully dried, Oxygen plasma (100 W power, 0.5 torr, 2 min) is used to etch the PMMA on the as-prepared sample, as shown in Step 7. Now we have the two layers Au triangle array. Repeating Step 4 to Step 7, multilayer (more than 2 layers) Au array can be prepared.

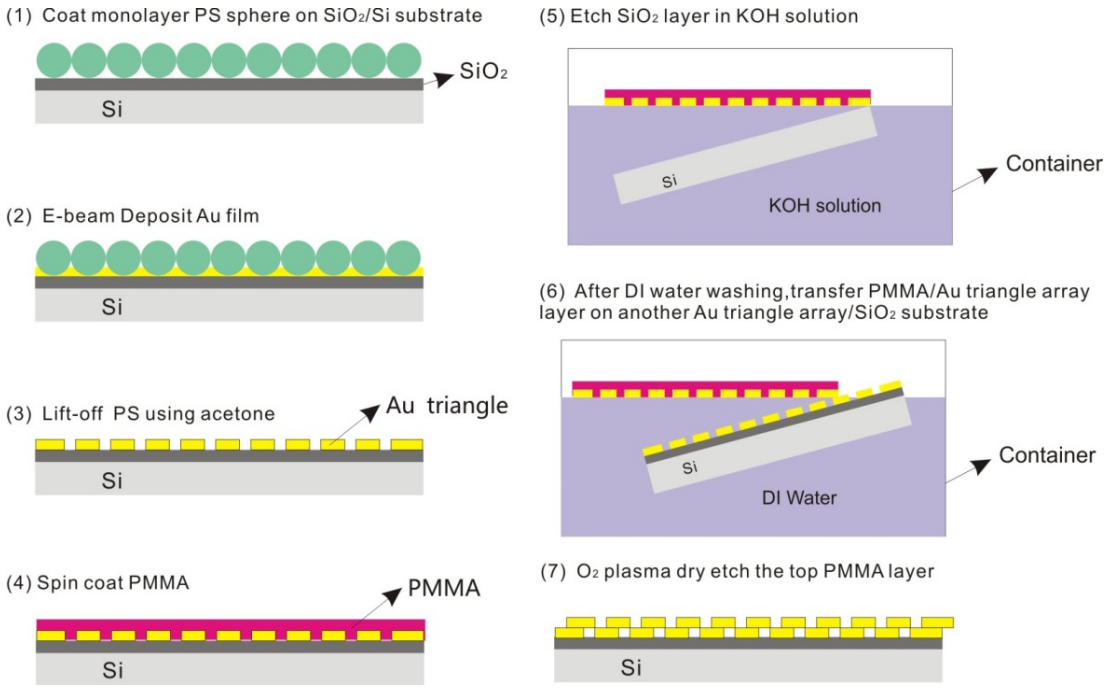

Figure 4.1 Schematic of fabrication of multilayer Au nanotriangle array.

Benzenethiol (BT) is used to characterize the SERS performance of multilayer Au triangle layer. BT is less sensitive to photo-bleaching and it has weak electronic interactions with metal surfaces as well as unimportant chemical enhancement.[58] BT also forms a self-assembled monolayer on metal surfaces.[64, 65] Therefore, BT is frequently used as a probe of electromagnetic enhancement. BT is adsorbed on the gold surface by soaking the Au triangle array sample in a 5 mM solution in ethanol for 30 min. The samples are then rinsed with ethanol, and left to dry in air for 15min.

FDTD simulation (Lumerical Solutions, Inc.) is employed to simulate the electric field around Au triangles for one and multilayer Au triangle array. The wavelength of excitation light is 633 nm. The amplitude $|E_0|$ of incident light is set to be 1. The calculated amplitude of electric field $|E|$ appears as the ratio of $|E|/|E_0|$. The local electric field enhancements depend strongly on the exact position of the SERS substrate surface. Thus, the SERS EFs on the surface of a typical SERS substrate are highly non-uniform down to nanometers scale. For trace amount molecule sensing, both hot spots and their size need to be considered for the evaluation of the overall SERS enhancement. To quantitatively characterize the overall SERS enhancement,[66] we apply an volume integral of $|E|^4$ value over a fixed space based on the commonly employed $|E|^4$-approximation.[17] The obtained result is the overall enhancement value used to evaluate the performance of various Au nanostructures.

4.3 Results and Discussion

4.3.1 Morphology of multilayer Au nanotriangle array

Morphology of multilayer Au nanotriangle arrays is investigated by SEM. Figure 4.2 shows the SEM images of monolayer and multilayer Au triangle array on SiO_2/Si substrates. Monolayer Au triangle array shows nearly periodical pattern (Figure 4.2(a)). After adding more layers, the pattern gradually loses periodicity (Figure 4.2(b-c)). In addition, more gaps between triangles are formed and the gap size becomes smaller with increasing number of layers. The yellow-boxed regions in Figure 4.2 indicate the small gaps formed in multilayer Au triangle array. It is also found

that more area of the SiO_2/Si substrate is covered by Au triangle as layer number increases.

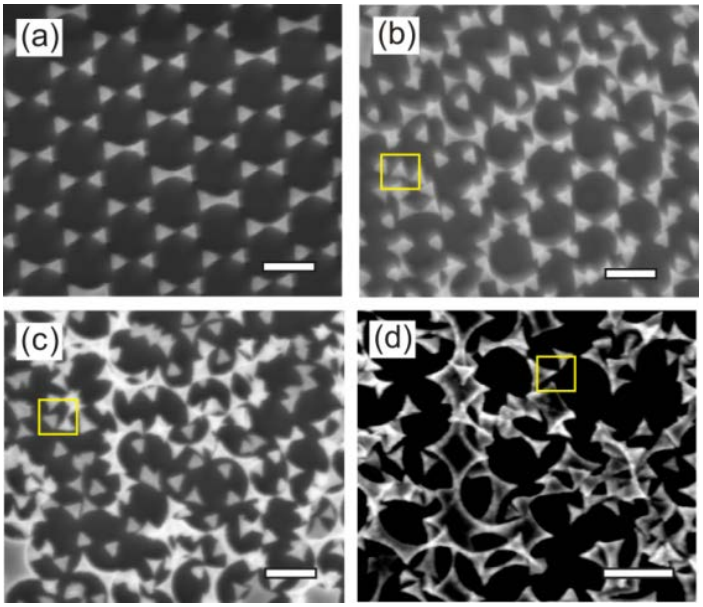

Figure 4.2 SEM image of (a) 1 layer, (b) 2 layers, (c) 3 layers and (d) 4 layers of Au nanotriangle array. Scale bars in the images are 500 nm. Yellow-boxed regions indicate the small gaps formed in multilayer Au triangle array.

To evaluate the SERS performance of multilayer Au triangle array, BT is used as analyte molecule. Figure 4.3 (a) shows the Raman spectra of BT on monolayer and multilayer Au triangle array. Take BT 1074 cm^{-1} peak intensity as a metric, it can be seen that the peak intensity measured on 4 layers triangle array is 2 orders of magnitude higher than that of the 1 layer triangle array. Figure 4.3 (b) shows the Raman mapping of BT 1074 cm^{-1} peak intensity on 1 layer and 4 layers Au triangle array. It can be seen that the density of the hot spots with intense SERS signal (>10,000 counts) of 4 layers Au triangle array is much higher than that of 1 layer Au triangle array.

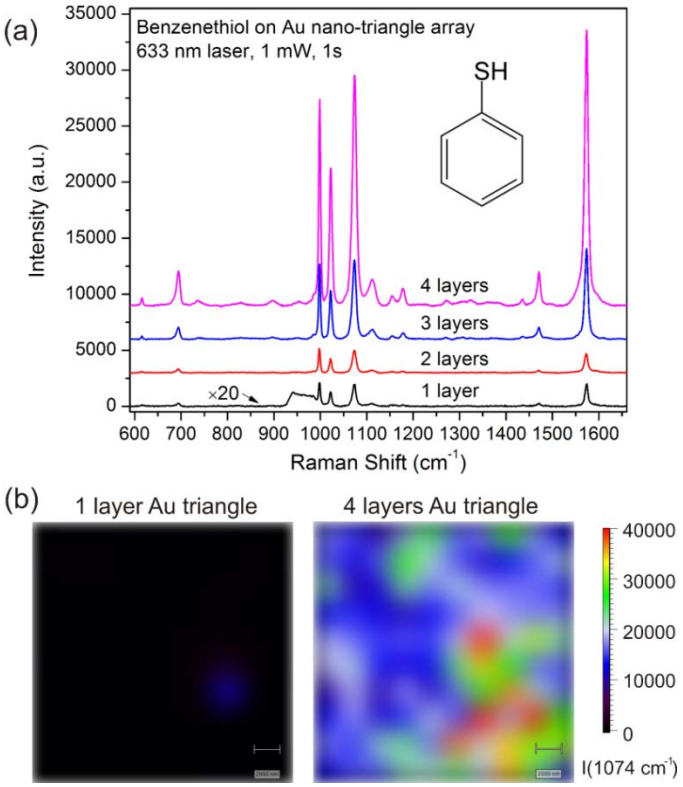

Figure 4.3 (a) Raman spectra of Benzenethiol measured on Au nanotriangle array with 633nm laser. Inset image in (a) shows the structure of benzenethiol molecule. (b) Raman mapping of 1074 cm^{-1} peak intensity on one-layer and four-layer Au triangle array. Scale bars in (b) are 2 μm. Raman spectrum measured on 1 layer Au triangle array in (a) is enlarged by 20 times (indicated by ×20). The large broad band signal from ~925 to 1000 cm^{-1} shown in the 1 layer substrate is the silicon second order Raman band.

4.3.2 SERS performance of multilayer Au nanotriangle array

Figure 4.4 shows the statistical distribution of BT 1074 cm^{-1} peak intensity measured on Au triangle arrays with different layer numbers. The datasets shown in Figure 4.4 are obtained by conducting three Raman mappings with more than 400 spots on the entire surface of each sample. This statistical distribution shows the overall SERS enhancement of substrates and the hot spots

density. Median in Figure 4.4 means the median intensity of BT 1074 cm^{-1} peak in the data points. Coefficient of variation (CV), which is defined as the ratio of the standard deviation to the mean, is used to measure the dispersion of a frequency distribution. As the number of layer increases, the increasing median indicates significant improvement of SERS signal intensity, and the decreasing CV suggests that the signal intensity becomes more concentrated near its median. In other words, by increasing the number of layers, we can achieve stronger Raman signal, as well as higher density of hot spots, indicating stronger and even more robust SERS enhancement. It can be observed that as layer number increases, the overall enhancement first increases and then decreases with maximum enhancement at 4 layers.

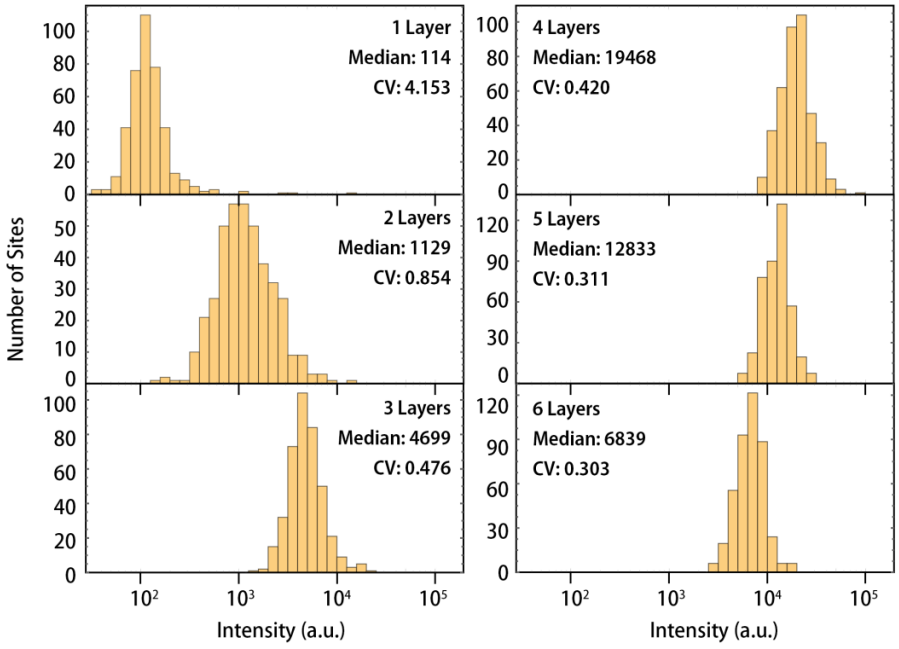

Figure 4.4 Statistical distributions of 1074 cm^{-1} peak intensity of 1, 2, 3, 4, 5 and 6 layer substrates. Numbers on x-axis in the histogram represent the Raman peak intensity.

4.3.3 Theoretical understanding of the SERS enhancement

To understand deeper how the number of layers affects the electromagnetic field enhancement, we employ FDTD simulation to investigate the local electric field distribution around Au triangles. Figure 4.5(a) and (b) show the electrical field mapping of 1 layer and 4 layers triangle array. It can be seen that as layer number increases, both the amount of hotspots and the electrical field intensity of the hotspots increase. We also observe that the gaps between the triangles, especially the narrower ones, are actually the major contributors of the SERS enhancement. The results point to the physical picture that the added layers can provide a great number of randomly distributed Au triangles on the original surface, narrowing the gap between triangles, increasing the number of gaps, and leading to substantial enhancement of SERS signal intensity and stability. An independent FDTD simulation (Figure 4.5(c)) of two Au nanotriangles confirms that smaller inter-particle gap width could generate larger overall SERS enhancement (integral of $|E|^4$ value over space), which further supports our arguments. This phenomenon has been observed and studied before[67] and our result is in accord with previous report. When the gap width start to decrease from 50 nm, the overall SERS enhancement increases quickly, pointing out that gaps narrower than 50nm are the major source of hot spots, which account for the enhanced SERS signal. Furthermore, we investigate the overall SERS enhancement of Au triangle array with different layers using FDTD. The simulation results are shown in Figure 4.5(d). It can be seen that as layer number increases, the overall enhancement first increases and then decreases with

maximum enhancement at 4 layers. It is worth noting that the multilayer effect observed in our experiment is different from the previous reported metal-dielectric-metal multilayer effect[68, 69]. In those reports[68, 69], the improved SERS performance in multilayer structure is mainly due to the dielectric layer separating the electrical field generated by two continuous Ag or Au film.

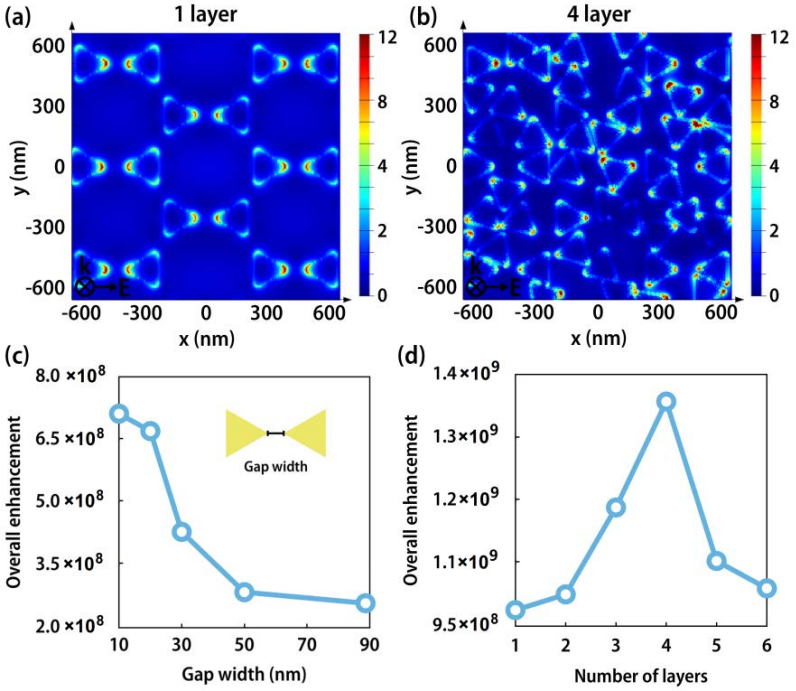

Figure 4.5 (a) and (b) show the 2-D electric field distribution given by FDTD simulation that corresponds to 1 layer model and 4 layers model respectively. (c) Overall SERS enhancement of two nearby triangles with increasing gap width given by FDTD simulation, showing that within our structure scale of about 10nm to 100nm, the narrower the gap, the stronger the SERS enhancement. Inset shows schematic of the model for simulation. (d) Overall SERS enhancement with different layers of Au triangle given by FDTD Solutions. Multilayer Au array models used for FDTD simulation are made by adding one Au array on another with random position and twisting angle.

In order to justify mathematically whether the amount of gaps would actually increase when additional layers are added. We perform a theoretical modeling for the multilayer triangle substrates, which would provide some profound statistical understanding of the results. Given that the gaps between two triangles play a major role in electric field enhancement, and the gaps are determined by nearby triangles, we locate the nearest neighbor (NN) and next nearest neighbor (NNN) for every single triangle. Figure 4.6 shows how we construct our model. Within an area of 10μm×10μm, each point represents the center of a triangle and the direction of the triangles are assigned in accordance with reality. Multilayer triangle array could be obtained simply by overlapping several layers with random position and twisting angle. A three-layer model is shown in Figure 4.6 (b) for example.

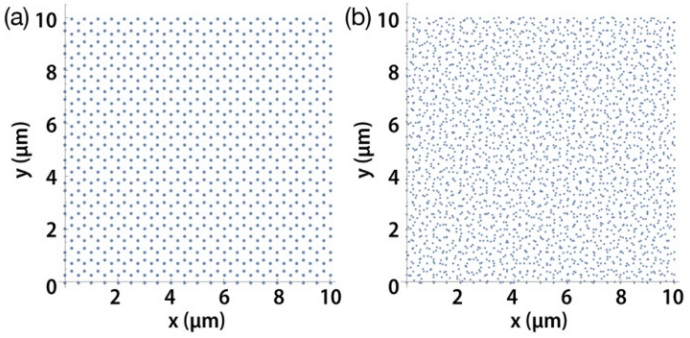

Figure 4.6 (a) Model for single layer substrate. (b) Model for 3-layer substrate

We calculate the gap width between neighboring triangles by subtracting the center-to-edge distance for two neighboring triangles from their center-to-center distance. The statistical results are shown in Table 4.1. The negative gap width means that two triangles are too close to form a gap for enhancement. Here we choose 50nm as a threshold for the aforementioned reason. The

trend given by this theoretical calculation confirms that the number of gaps will indeed increase as layer number increases from 1 to 4, and then decrease when layer number further increases. The statistical results are in accord with FDTD simulation and our experimental observation that 4 layers Au triangle array provides the optimum SERS performance.

Table 4.1 Statistical results of simulation

Number of layers	2	3	4	5	6
number of gaps	868	2560	4543	6887	9156
number of gaps	804	1644	2159	2040	1830

4.4 Conclusion

In conclusion, we conduct a systematic study on a practical way of patterning metallic nanostructures for achieving high SERS EFs and high hot spot density. By superimposing one layer Au triangle array on another to form multilayer triangle array, SERS signal can be enhanced by two orders of magnitude. We also develop the physical understanding of the SERS enhancement of multilayer triangle array. The drastic increased SERS EFs and the hot spot density are due to the increase of the amount of gaps formed between Au triangles and the decrease of the gap size. We find that the optimum layer number for Au triangle array studied in this work is 4 layers through FDTD simulation and theoretical analysis. The patterning method here can be used to form multilayer nano-array with other shapes in order to achieve ultra-strong local electromagnetic field.

Chapter 5 Spectroscopic Study of MoS_2/Au Plasmonic Nanostructure

5.1 Introduction

Most SERS researches are based on metallic nanostructures that can provide intense local electric field. In addition to the traditional metallic nanostructures, van de Waals materials, such as graphene and molybdenum disulfide (MoS_2), have been explored to enhance Raman signal.[5, 37-39] The SERS effect of van de Waals materials is mainly due to the chemical enhancement. This chapter discusses a serendipitous discovery about bilayer MoS_2 spectral features when we investigated the use of MoS_2 as a potential SERS substrate. The chapter presents combined spectroscopic studies of CVD grown bilayer MoS_2 of 0° (AB stacking) and 60° stacking (AA' stacking) with clear differences in both Raman and PL spectra. The studies are enabled by the drastically enhanced signal-to-noise (S/N) ratios derived from plasmon resonance of Au nanopyramid SERS substrates.

MoS_2 is a member of layered transition-metal dichalcogenides (TMD) with a number of highly interesting physical properties. The indirect band gap of 1.2 eV in the bulk form evolves with decreasing number of layers and becomes direct band gap of 1.9 eV in monolayer MoS_2.[70-72] In many senses, the most unique property of TMD family of materials consisting of combinations of Mo, W, S, and Se is the strong spin-orbit coupling.[73] This originates from the d-orbitals of the heavy elements (Mo and W)[45] and offers exciting opportunities for device applications leveraging spin and valley degree of freedom.[74-76] Compared to the more studied monolayer TMDs, bilayer

structures offer an added layer-degree of freedom. Interactions between MoS_2 layers as well as the specific stacking order can significantly modify their electrical,[77] optical[72] and vibrational properties.[78] The specific spin-orbit based behavior depends sensitively on crystal symmetry as elucidated by many theoretical studies.[73, 79] Robust valley polarization is assured by the lacking of centro-symmetry in all monolayer TMDs as well as bilayer ones with AB stacking.[74] Furthermore, inter-layer hopping has been shown to be significantly suppressed by the strong coupling between spin and valley-pseudospin as well as layer-pseudospin[80-82] allowing for the signatures of different spin-, valley, and layer- states to be experimentally observed. We report the results of combined optical spectroscopy and electron microscopy studies on AA' and AB stacked bilayer MoS_2 shedding lights on potential challenges of device applications.

Many insightful experimental studies have appeared in the literature in the past couple of years.[74-76, 83, 84] Recent study[74, 85] on spin polarization in MoS_2 also addressed the importance of stacking order between adjacent MoS_2 layer on spin/valley polarization. Interlayer interaction between adjacent MoS_2 layers with different stacking order has been investigated through stacking two CVD grown monolayer MoS_2 with a range of different twisting angles,[86, 87] or CVD grown bilayer MoS_2.[88] These reports show clear stacking angle dependence of optical properties of bilayer MoS_2.[86-88] However, in these reports, there is no mentioning of the spectral differences between bilayer MoS_2 with 0° and 60° stacking angle, which correspond to the natural phases of MoS_2, 3R and 2H respectively.[86] To date, only one of the experimental results[83] showed the

difference between the photoluminescence (PL) spectra of 2H and 3R bulk MoS_2 with Cl_2 molecules intercalated between MoS_2 layers. In this chapter, we present for the first time combined spectroscopy studies of bilayer MoS_2 of 0° (AB stacking) and 60° stacking (AA' stacking) with clear differences in both Raman and PL spectra.

5.2 Experimental

5.2.1 CVD Grown MoS_2 Atomic Layer

MoS_2 bilayer sample is prepared using the same method reported in ref.[89] To synthesize MoS_2 atomic layers in a vapour phase deposition process, MoO_3 and pure sulphur are used as precursor and reactant materials, respectively. SiO_2/Si (300nm thick SiO_2) substrates are used. CVD depositions are performed at the reaction temperature of 850 C°. Bilayer MoS_2 are transferred onto Au tipped surface *via* a standard PMMA-based transfer approach. MoS_2 bilayer samples on SiO_2/Si substrates are spin-coated with PMMA layer (950 PMMA A4 from Microchem) with a spinning speed of 2000 rpm for 1 min and submerged in KOH solution. Subsequently, PMMA/MoS_2 film is cleaned by DI water and then transferred onto Au tipped surface. To avoid MoS_2 layers from being washed away, PMMA layer (about 200 nm thickness) is not removed from the transferred MoS_2. STEM samples are prepared using similar method used in MoS_2/Au pyramid sample. The only difference is that the PMMA protecting layer is removed with acetone following the transfer.

5.2.2 Fabrication of Au Nanopyramids

The Au nanopyramid fabrication is based on sphere-lithography.[60] Figure 5.1 shows the fabrication process. Firstly, polystyrene (PS) nano-spheres (500 nm in diameter, Alfa Aesar) are coated on SiO_2 (50 nm)/Si wafer using scooping transfer method.[90] Before coating PS spheres, SiO_2/Si wafer is washed by Piranha solution (H_2SO_4:H_2O_2=3:1(volume ratio)) for 1h at 70 °C followed by de-ionized water (DI water) rinsing for 3 times. In scooping transfer process, a few drops of the diluted PS sphere suspension (5% aqueous PS sphere suspension mixed with an equal volume of ethanol) are introduced on the water surface using the partially immersed glass slide (2 cm × 10 cm). The glass slide is pretreated by a Piranha solution for 1 h at 70 °C and then rinsed by DI water for 3 times. After introducing PS spheres on the water surface, PS spheres will self-assembly and form closed-packed monolayers with hexagonal patterns. When about 80% of the water surface is covered with PS spheres, PS monolayer is transferred on SiO_2/Si substrates using simple scooping transfer method. Figure 5.2 (a) shows the SEM image of the PS spheres coated on SiO_2/Si substrate. The PS spheres/SiO_2/Si sample is then dry-etched by O_2 plasma (200W power, 50s) to reduce the size of PS sphere to about 250 nm (Figure 5.2 (b)).

After etching PS spheres, 50 nm Cr film is deposited on the as-prepared sample using electron beam deposition (Figure 5.1 step (3)). The PS spheres are then lift-off by ultra-sonicating the sample in acetone for 20 min, followed by DI water rinsing for 3 times. Figure 5.2 (c) shows the SEM image of the sample after PS lift-off. Using the Cr film (with small holes in the film) as mask,

the 50 nm SiO_2 film beneath the Cr film is dry-etched by Oxford Plasmalab Plasma Etcher (25 sccm Ar, 25 sccm CHF_3, RIE power 200W, etch time 2min).

After etching SiO_2, the hole pattern is transferred on SiO_2 from Cr film. The sample is then etched in KOH aqueous solution (60 wt%) for 2 min at 60 °C to form pyramidal structure on Si surface (Figure 5.2(d)). The whole sample is then immersed into HF solution (30%) to remove SiO_2 and Cr layer. At this time, Si pyramidal mold (Figure 5.2(e)) fabrication has been finished. 200 nm Au film is deposited on the Si mode with pyramidal structure by sputtering. 5-min epoxy is used to glue the Au film on another SiO_2 (300 nm)/Si substrate, which is used to hold the Au nano-pyramids. After the epoxy cured at the room temperature, Au nano-pyramids are peeled off (Figure 5.1 step (9)).

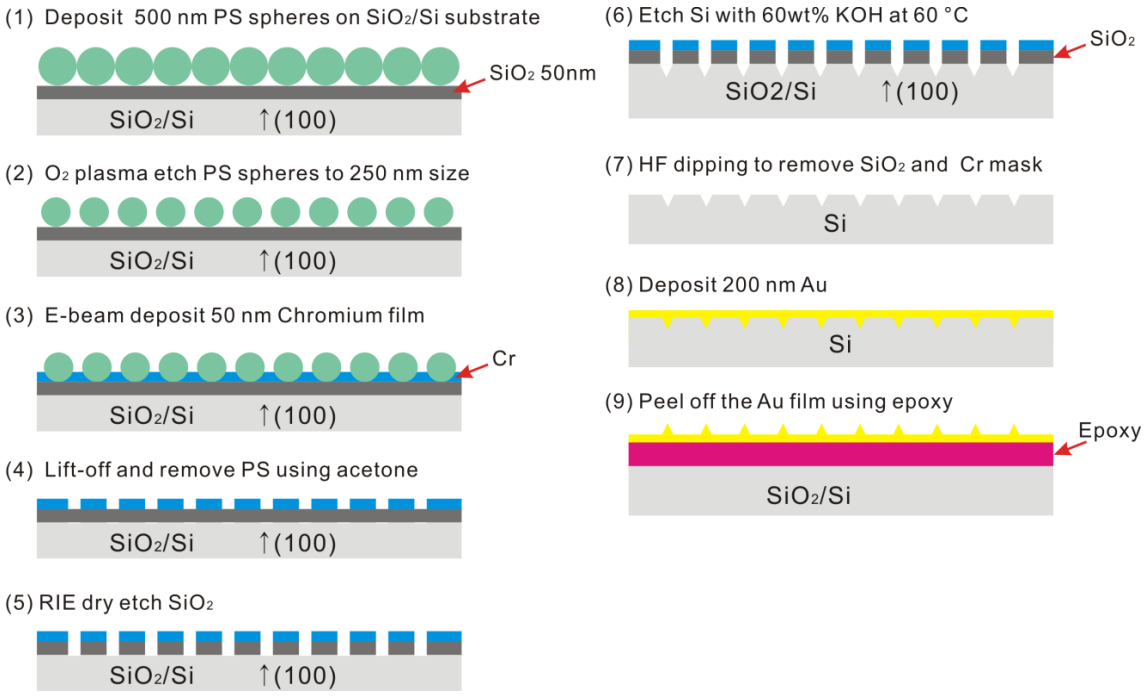

Figure 5.1 Schematic of the graphene/Au tip hybrid platform fabrication process.

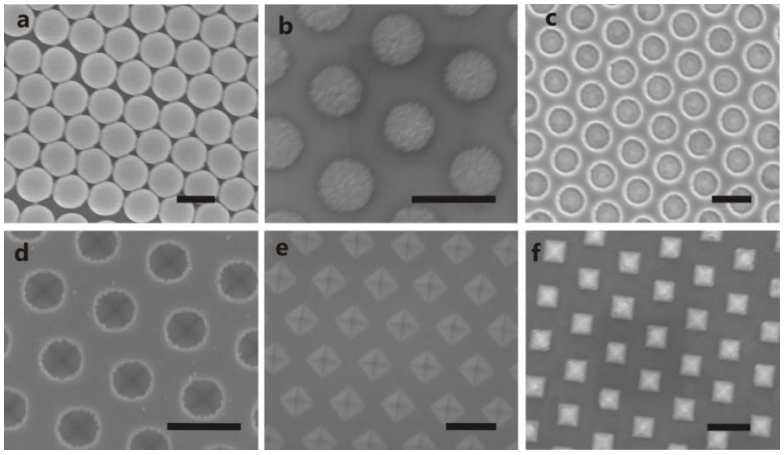

Figure 5.2 (a) SEM image of PS spheres on SiO_2/Si substrate. (b) SEM image of PS spheres after O_2 plasma etching for 50s. (c) SEM image of the Cr/SiO_2/Si sample after PS lift-off. (d) SEM image of the Cr/SiO_2/Si sample after KOH etching. (e) SEM image of Si surface with inverse pyramidal hole. (f) SEM image Au nano-pyramids.

5.2.3 Micro-Raman and Photoluminescence Measurement of MoS_2

Micro-PL measurements are performed in backscattering geometry using a CW laser at 532 nm wavelength and a 50× IR objective lens with N.A.= 0.65 (Olympus microscope). The excitation power at the sample surface is in the 0.5-2 mW range. Sample temperature is kept at 300 K using a Linkam cryostat. PL emission is dispersed by a Horiba iHR320 spectrometer and detected by a 256x1024 pixel Si CCD detector. The spectrometer is calibrated daily against reference emission and laser satellites. PL data have been normalized to the spectral response of the entire experimental set-up measured by means of a calibrated light source.

Raman spectra are measured using Renishaw inVia microscope under 633 nm laser excitation.

The laser power used is 0.5 mW. The grating used is 1800 l/mm and the objective lens used is 100×. A step size of 200nm is used for Raman mapping. Raman data is analyzed using Renishaw WiRE 3.2 software.

5.2.4 Scanning TEM (STEM) Analyses

STEM experiments are performed with the Nion UltraSTEM, a dedicated STEM equipped with a cold field emission electron source and a corrector of third and fifth order aberrations, operating at 60 kV accelerating voltage.

5.3 Results and Discussion

5.3.1 FDTD Simulation of EM Field Distribution around Individual Au Pyramids

Plasmonic surface used in the experiment is Au nano-pyramid structure, which is fabricated by sphere-lithography.[43] Plasmon resonance on the Au nano-pyramid surface has been shown to enhance the Raman signal of molecules by up to seven orders of magnitude.[5, 43] Another unique feature of the Au nano-pyramid plasmonic surface is the out-of-plane electric field (E-field) component of nearly the same intensity as the in-plane component near Au pyramid surface.

FDTD simulation is conducted using Lumerical software (FDTD Solutions 8.11).[56] Figure 5.3 shows the 3D model used. Au pyramid has a bottom length of ~250 nm with ~500 nm pitch. The continuous Au flat film (on the bottom of Au pyramids) thickness is ~20 nm. Figure 5.4 shows the 3D distribution of the electrical component of the EM-field around individual Au tips.

The simulation space is indicated by the yellow cubic shown in Figure 5.3. Figure 5.4 (a) shows the 3D distribution of the electrical component of the EM-field symbolized with blue arrows with the cross-sectional views along three major symmetry planes being presented in Figure 5.4 (b-d). Figure 5.4 (b-d) shows the projections of the electrical field on the Y-Z, X-Z, and X-Y planes, respectively. Red dashed line shows the ridges of the Au pyramid. E-field is not parallel to X-direction near Au pyramid surface. The fact that the electrical component of the EM field possessing significant out-of-plane components can be clearly seen in Figure 5.4 (b, c).

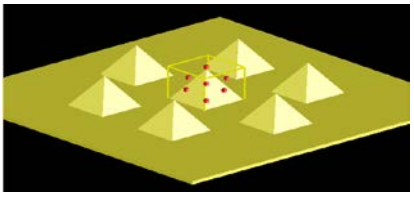

Figure 5.3 Au pyramid model used for FDTD simulation.

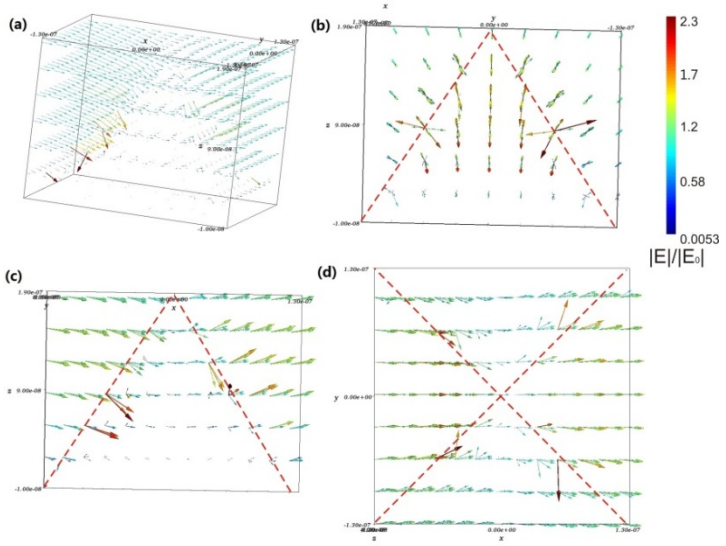

Figure 5.4 (a) 3D E-field distribution around an Au pyramid. E-field projection on Y-Z (b), X-Z (c), X-Y (d) plane. Red dashed line shows the ridges of Au pyramid.

5.3.2 TEM Analysis of Bilayer MoS_2

Bilayer MoS_2 with different stacking orders in this study is grown by CVD and transferred on Au plasmonic surface for optical studies. CVD grown bilayer MoS_2 in our experiments typically show two kinds of microscopic shapes, one with 0° twist angle between the two layers (AB stacking), while the other with 60° twist angle (AA' stacking), as shown in Figures 5.5 (a) and (h), respectively. Although many theoretical studies[85, 91] have illustrated the possible atomic configurations in bilayer MoS_2 with the two different stacking orders, few experiments have been done on atomic scale. In this study, scanning transmission electron microscopy (STEM) was employed to establish the correlation between the atomic arrangement and the microscopic shape of the bilayer islands. The contrast of STEM high angle annular dark field (STEM-HAADF) image is sensitive to the atomic number and sample thickness, which makes it possible to identify the detailed atomic arrangement. Figures 5.5 (c) and 1(j) show two typical STEM-HAADF images of the boundary regions between monolayer and bilayer MoS_2. The Mo and S atoms in monolayer can be unambiguously distinguished due to their obvious large difference in atomic numbers. To correctly interpret our bilayer STEM images, QSTEM simulation package[92, 93] is employed. Through comparing the experimental with the simulated STEM images, we can deduce the real atomic configurations of the bilayer MoS_2 samples. Figure 5.5(d) is the enlarged red-boxed region of the experimental image from the bilayer region of the sample with 0° twist angle as shown in Figure 5.5(c). Figure 5.5(f) is the simulated STEM image of the atomic configuration shown in

Figure 5.5(b), *i.e.* AB stacked bilayer MoS_2. It can be seen that Figure 5.5(f) is identical to Figure 5.5(d). Furthermore, the experimental intensity profile shown in Figure 5.5(e) is nearly identical to the simulated intensity profile shown in Figure 5.5(g). Therefore, it can be deduced that Figure 5.5(d) has the same atomic configuration as shown in Figure 5.5(b), *i.e.* AB stacked bilayer MoS_2. In the same way, we can get that Figure 5.5(k), the enlarged red-boxed region of the experimental image from the bilayer region of the sample with 60° twist angle as shown in Figure 5.5(j), has the same atomic configuration as shown in Figure 5.5(i), *i.e.* AA' stacked bilayer MoS_2. Our STEM results lend strong support to the assignment of the bilayer MoS_2 with 0° twist angle being of AB stacking order whereas that with 60° twist angle being of AA' stacking order.

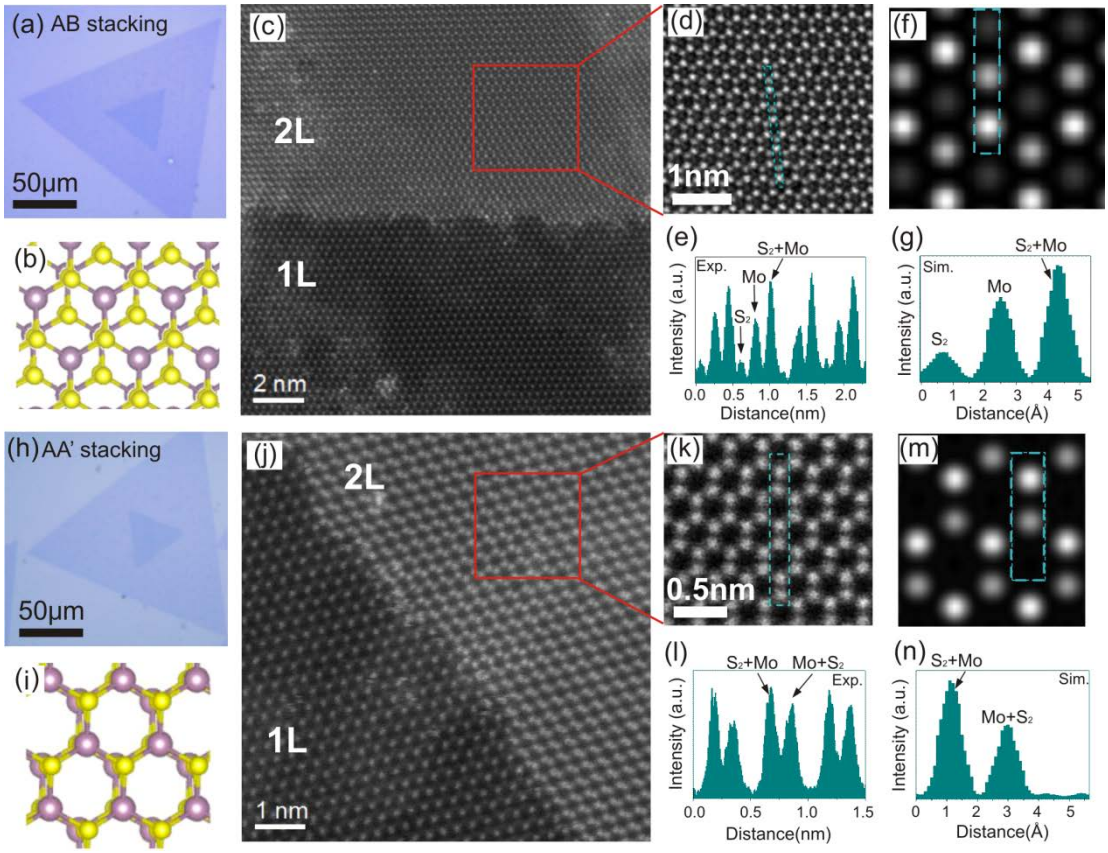

Figure 5.5 (a) Optical image and (b) atomic configuration of AB stacked bilayer MoS_2. (c) STEM-HAADF image of the boundary between AB stacked bilayer and mono-layer MoS_2. (d) Magnified image of the red-boxed area in (c). (e) Intensity profile of the selected line (bright cyan) in (d). (f) Simulated STEM-HAADF image and (g) simulated intensity profile of the selected line (bright cyan) in (f). (h) Optical image and (i) atomic configuration of AA' stacked bilayer MoS_2. (j) STEM-HAADF image of the boundary between AA' stacked bilayer and mono-layer MoS_2. (k) Magnified image of the red-boxed area in (j). (l) Intensity profile of the selected line (bright cyan) in (k). (m) Simulated STEM-HAADF image and (n) simulated intensity profile of the selected line (bright cyan) in (m). Purple balls in (b) and (i) represent Mo atoms while yellow balls represent S atoms.

5.3.3 Resonance Raman Measurement of Bilayer MoS_2 on Au Nanopyramid

Raman spectroscopy has proven to be a powerful tool to study the optical response of 2D van der Waals materials like graphene.[94] For MoS_2 atomic layers, Raman spectroscopy shows clear evolution trend of A_{1g} and E^1_{2g} peak position with layer thickness.[78, 95] As layer thickness increases, A_{1g} peak position blue shifts while E^1_{2g} peak red shifts.[78, 95] Compared with the first-order process in normal Raman scattering, resonance Raman scattering enhances the possibility of higher order Raman scattering resulting in enriched spectral information. Resonance Raman scattering happens for a system when the incident laser excitation energy overlaps with (or is close to) the electronic bandgap energy. In this study, the resonance condition was achieved by exciting the sample with 633 nm laser (1.96 eV photon energy). Previous resonance Raman study of atomically thin MoS_2

layers at room temperature[96] suffers from low signal to noise ratio due to the typically low Raman yield. This shortcoming of Raman spectroscopy can be overcome with the help of surface plasmon resonance, *i.e.* SERS. In our study, we employ a specific type of plasmonic surface, Au nano-pyramid plasmonic substrates (Figure 5.6 (b)), to boost the Raman signal of MoS_2 layers.

The resonance Raman spectra of AA' and AB stacked bilayer MoS_2 measured on Au nano-pyramid substrates are shown in Figure 5.6(a). The inset optical image in Figure 5.6(a) shows two types of bilayer MoS_2 on Au nano-pyramid substrates. Two major peaks, E_g (385 cm^{-1}) and A_{1g} (405 cm^{-1}) can be identified in the spectra. E_g symmetry band in the AA' stacked bilayer corresponds to E_{2g} symmetry band in the 2H bulk MoS_2.[97] E_g peak represents vibration of Mo and S atoms in the basal plane; whereas in A_{1g} vibrational configuration, Mo atoms remain fixed and only S atoms vibrate along the c-axis. The new Raman peaks, which are not commonly observed with the 514 or 532 nm laser lines, are assigned based on resonant Raman of bulk MoS_2.[84] Raman peak at 179 cm^{-1} is assigned to a difference combination mode of A_{1g}(M)–LA'(M), where LA'(M) mode (233 cm^{-1}) is quasi-longitudinal acoustic (LA') mode at M point of Brillion Zone.[84] The peak at 420 cm^{-1}, commonly known as "b" peak, is assigned to a two-phonon process and the appearance of this mode is related to the A exciton at the K point.[98] The peak located at ~460 cm^{-1} is asymmetrical and can be viewed as being composed of two parts. The lower frequency part of this peak is due to a van Hove singularity between K and M point of Brillion Zone and the higher frequency part is mostly due to the LA and LA' phonons at M point. The peaks at 526 cm^{-1}, 571

cm^{-1}, 599 cm^{-1} and 642 cm^{-1} are assigned to (i) E_g(M) + TA'(M), (ii) A_{1g}(M)+TA'(M), (iii) E_g (M)+LA'(M), and (iv) A_{1g}(M)+ LA'(M) respectively. TA' (M) is quasi-transverse acoustic (TA') mode at M point of Brillion Zone. For comparison, resonance Raman spectra of MoS_2 on flat Au surface and SiO_2/Si substrates are shown in Figure 5.6 (d). The S/N ratios of Raman spectra of MoS_2 on both flat Au surface and SiO_2/Si substrates are lower than those on Au nano-pyramids. It can be seen that the major Raman peak positions and shapes of MoS_2 on flat Au surface are similar to those on Au nano-pyramids. Although the Raman spectral shapes of AA' and AB stacked bilayer MoS_2 on SiO_2/Si substrates appear to be different, these features varies among different samples with the same stacking order. As such, the Raman spectral shape is not an identifying feature of the MoS_2 stacking order. SERS enhancement factors (EFs) calculated for MoS_2 bilayer is on the order of 10^5. SERS EF represents the extent the Raman signal is boosted comparing to regular Raman. In this study, SERS enhancement is mainly due to the electromagnetic (EM) enhancement mechanism. As such, SERS EF could be used as a figure of merit to measure the extent of plasmon resonance of Au nano-pyramids referenced to either the flat Au surface or the SiO_2 surface.

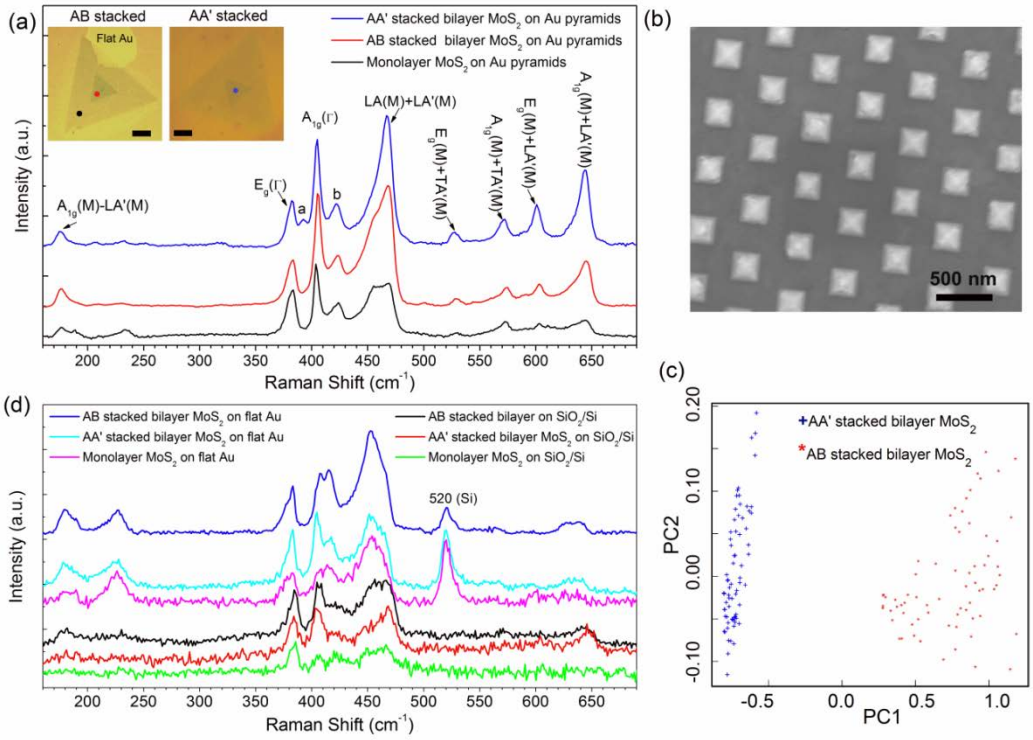

Figure 5.6 (a) Resonance Raman spectra of monolayer and bilayer MoS_2 on Au nano-pyramids. The blue, red and black spectrum were obtained at the spots with the same color in the samples shown in the inset optical image. The inset optical image shows the AA' and AB stacked bilayer MoS_2 on Au nano-pyramids (The Au nano-pyramid substrates contain some interdispersed flat Au regions). The scale bars in the inset image are 50μm. (b) SEM image of Au nano-pyramid SERS substrate. (c) PCA diagram of AA' and AB stacked bilayer MoS_2 resonance Raman data. (d) Resonance Raman spectra of monolayer and bilayer MoS_2 on flat Au substrates and SiO_2/Si substrates. The Raman spectra were measured at 300 K.

The high S/N ratio renders clear spectral differences between AA' and AB stacked bilayer MoS_2. The primary difference is the appearance of the 395 cm^{-1} peak in AA' stacked bilayer MoS_2.

Among all the bilayer samples (more than 10 samples for each phase) measured, the 395 cm^{-1} peak only appears in Raman spectra of AA' stacked bilayer, never in those of AB stacked bilayer. This 395 cm^{-1} mode has been observed for 2H bulk MoS_2 using Resonance Raman spectroscopy at low temperature, and was named "a" peak.[99, 100] Livneh *et al.*[84, 99] found that in bulk MoS_2 this mode is constructed from two contributions, which are particularly distinguishable at low temperatures. The two contributions that construct "a" mode are assigned as LA'(M)+TA'(M) and LA(M)+TA(M).[84] To obtain quantifiable measure of the spectral differences, we employ principal components analysis (PCA).[101] PCA is a statistical procedure widely used in analyzing Raman spectra to identify spectral differences between datasets. PCA transforms the dimensionality of a data matrix, *e.g.* intensity versus wavenumber, to a new set of orthogonal variables that have the strongest correlations with distinctive spectral features. The new set of variables is known as principal components (PCs). Plots of one PC against another provide quantitative information about how different the datasets are in terms of sensitivity, specificity, *etc.* Figure 5.6(c) shows the PCA diagram of bilayer MoS_2 resonance Raman data. It can be seen that the Raman data corresponding to the two different stacking orders are distinctively different in the space of principal components.

To study the variation of the "a" peak within one bilayer sample, Raman mapping is conducted. Figures 5.7 (b) and (d) show the stacked resonance Raman spectra measured from AA' (Figure 5.7(a)) and AB stacked bilayer sample (Figure 5.7(c)) at room temperature, respectively.

Among the spectra measured from AA' stacked bilayer sample, the "a" peak always exists. However, this peak never appears in any of the AB stacked bilayer resonance Raman spectra. We also conducte variable temperature Raman measurements of bilayer MoS_2 on Au nano-pyramid structure. As shown in Figure 5.8, the key features of the bilayer Raman spectra do not show noticeable temperature dependence. More importantly, the "a" mode persists in the AA' (2H or 60° stacking) stacked bilayer at temperatures ranging from 293K to 77K but remains absent from the AB (3R or 0° stacking) stacked bilayer across the same temperature range. Interestingly, for AA' stacked bilayer MoS_2 we do not observe that "a" peak separated into two parts as temperature decreased from 293K to 77K, which is different from the situation for 2H bulk MoS_2.[84] This may be due to the reduced symmetry of AA' stacked bilayer MoS_2 (D_{3d}) compared with 2H bulk MoS_2 (D_{6h}). Considering that the "a" peak position is located at ~395 cm^{-1} in our case, it could be assigned as TA'(M) +LA'(M) according to Ref [84]. The SERS results suggest that this "a" peak could act as a Raman fingerprint to differentiate the two types of MoS_2 bilayers. A quantitative understanding of the Raman spectral differences would require theoretical calculations of phonon dispersion and density of states for two different MoS_2 phases. We hope that our results will motivate such calculations in future. Our findings provide two additional methods (in addition to low temperature photoluminescence [83]) for definitive determination of bilayer MoS_2 stacking orders, namely optical microscopy for isolated islands and SERS.

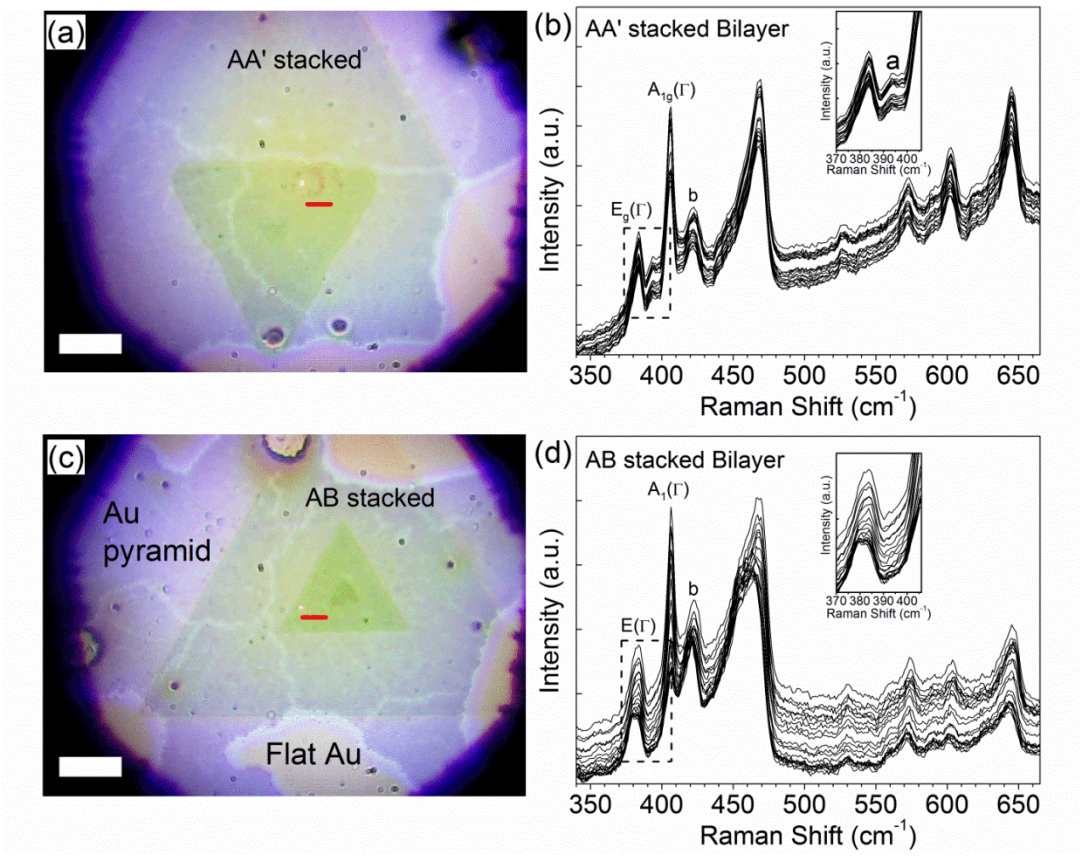

Figure 5.7 (a) Optical image of a AB stacked bilayer MoS_2 sheet on Au nano-pyramids. (b) Raman spectra obtained from line mapping (red line in (a)) with z-axis offset. (c) The optical image of a AA' stacked bilayer MoS_2 sheet on Au nano-pyramids. (d) Raman spectra obtained from line mapping (red line in (c)) with z-axis offset. The meandering lines and other features in the background are due to the in-homogeneity of our nano-patterning process. The scale bars in (a) and (c) are 10 μm. The Raman spectra shown in (b) and (d) are original spectra without background subtraction and were measured at 300 K. The inset figures in (b) and (d) are the enlarged spectra between 370 and 410 cm^{-1}. It can be seen that "a" peak appears only in the AA' stacked bilayer sample.

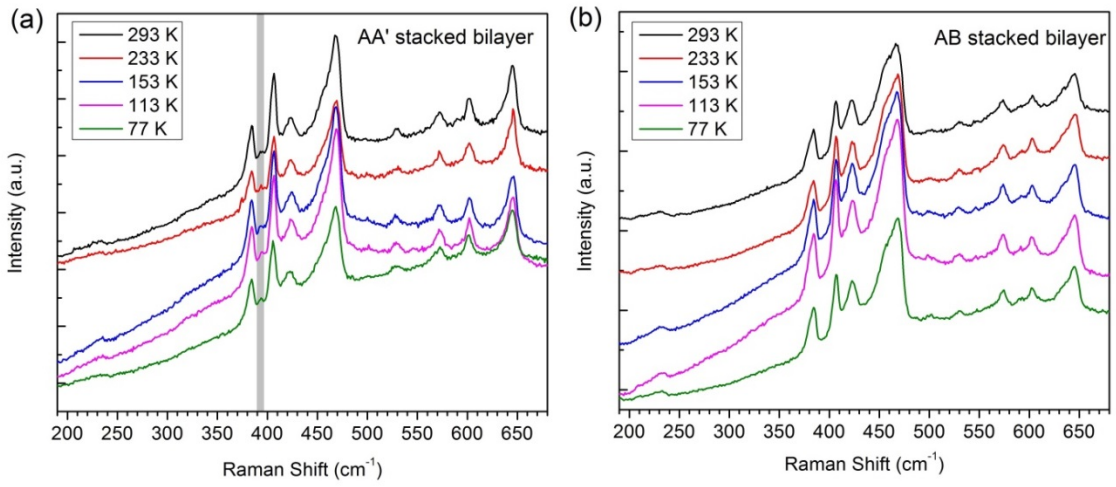

Figure 5.8 Resonance Raman spectra of (a) AA' and (b) AB stacked bilayer MoS_2 on Au nano-pyramid substrate at different temperature. Gray bar in (a) indicates the position of "a" peak.

5.3.4 Photoluminescence Study of Bilayer MoS_2 on Au Nanopyramid

In addition to the phonon vibrations, the electronic band structure of MoS_2 bilayers was investigated using PL. PL spectra of both monolayer and bilayer MoS_2 on Au nano-pyramids are shown in Figure 5.9 (a-c). A- and B-peak represent the direct-gap transitions and I-peak in bilayer MoS_2 PL spectra represents the indirect-gap transition. A^--peak is the trion peak.[87, 102] Au nano-pyramid substrate enhances the PL peak intensity by two orders of magnitude compared with PL of MoS_2 on flat Au surface (Figure 5.9(e)), and by almost one order of magnitude compared with that on SiO_2/Si substrate (Figure 5.9(d)). It is also observed that peak intensity of MoS_2 PL spectra measured on SiO_2/Si substrate is higher than those on flat Au surface. In the PL spectra of MoS_2 on both flat Au surface and SiO_2 surface, A^--peak is not clearly observed, and I peak

intensity of bilayer is very weak and non-discernable compared with the strong I peak intensity observed on Au nano-pyramid substrate. The physical origin of the strong I-peak intensity observed on Au nano-pyramid substrate is yet to be understood and warrants further studies. The enhanced S/N ratio provided by Au tipped surface allows for the observation of more spectral details. The most prominent difference between monolayer and bilayer MoS_2 is the strong I-peak in bilayer MoS_2. For bilayer MoS_2, the primary PL spectral difference between AA' and AB stacked bilayer is the I-peak position. A noticeable blue shift of the I-peak of AA' stacked bilayer by 0.056±0.017eV over that of the AB stacked bilayer was observed. This observation agrees with the DFT calculation findings of He *et al*.[77] in terms of the general trend but being different in value (0.06 eV from our PL study versus the 0.14 eV from DFT calculations). Previous experimental results[86, 88] did not address the difference between I-peak positions of AA' and AB stacked bilayer MoS_2. In addition, I/A peak intensity ratio in PL spectra obtained on Au pyramid region is higher than previous experiment results obtained on SiO_2/Si substrates.[86, 88] The emergence of the indirect band gap results from the interlayer electronic coupling. In bilayer MoS_2 band structure, doubly degenerate valence band splits into more branches near the Γ point and the upper branch reaches an energy value higher than the valence band at the K point in monolayer MoS_2. It has been suggested that the indirect band gap being an indicator of the interlayer electronic coupling strength with lower indirect band gap being correlated to higher coupling strength.[88] Our PL results indicate stronger interlayer electronic coupling in AB stacked bilayer MoS_2 over that of AA'

stacked bilayer. The electronic coupling is significantly affected by the separation between layers.[88] It is mainly defined by the orbital overlap of the inner sulfur atoms from the adjacent MoS_2 layers[86] with smaller interlayer distance leading to stronger electronic coupling.[86, 88] Both DFT calculation[77, 86] and experimental data[103] show that AB stacked bilayer MoS_2 has a smaller interlayer distance than AA' stacked bilayer. These findings support our finding. The difference between indirect gap energy in the two MoS_2 phases can also be understood from the perspective of electronic band splitting. DFT simulation results[77] show that AB stacked bilayer MoS_2 has additional band splitting over that of AA' stacked bilayer. Because of the lack of centro-symmetry in AB stacking, four bands are formed (instead of two in AA' stacking) along the M-K-Γ direction in AB stacked bilayer Brillouin zone. The band splitting causes lower indirect band gap in AB stacked bilayer MoS_2.

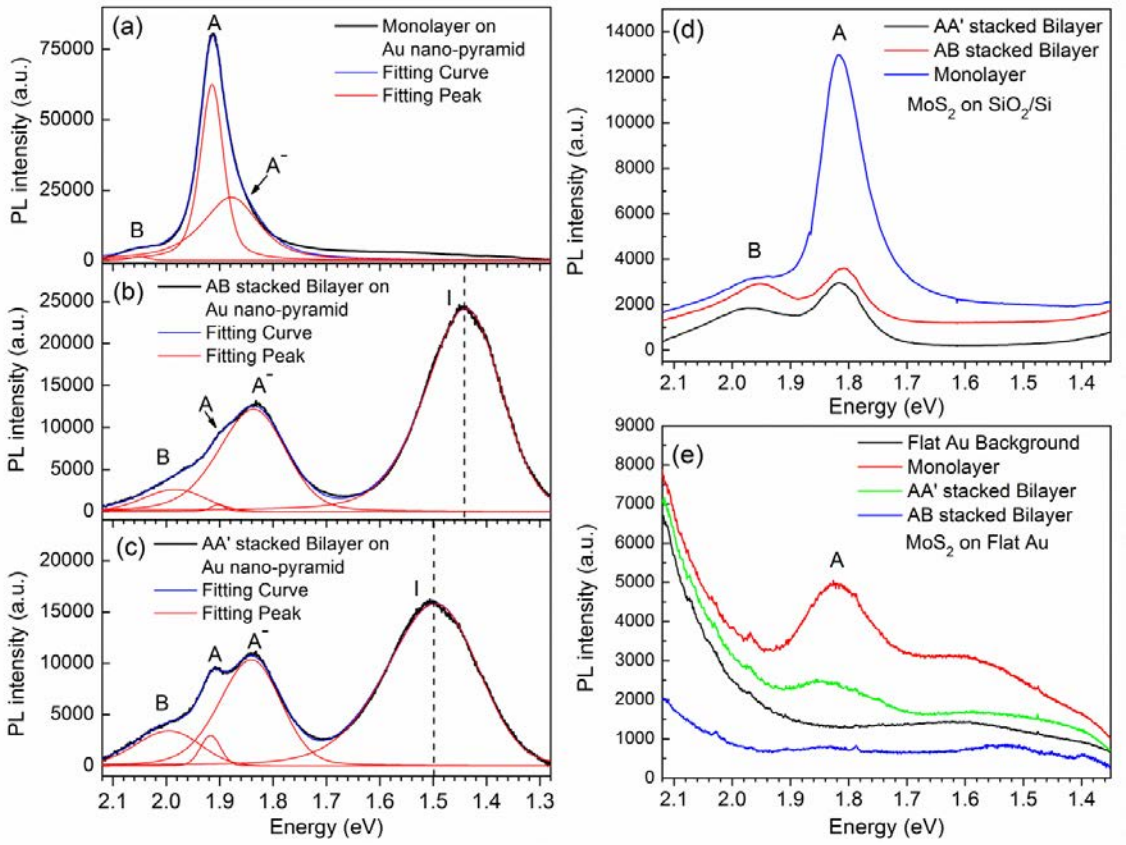

Figure 5.9 PL spectra of MoS_2 on Au nano-pyramid substrates: (a) Monolayer MoS_2, (b) AB stacked bilayer MoS_2, and (c) AA' stacked bilayer MoS_2. (d) PL spectra of MoS_2 on SiO_2/Si substrates. (e) PL spectra of MoS_2 on flat Au substrates. 532 nm laser (0.8 mW power) was used for PL measurement at 300K.

It can be noticed from Figure 5.9 (b) and (c) that A^-/A peak intensity ratio of PL spectra of AA' and AB stacked bilayer MoS_2 is different. However, this peak intensity ratio is not unique to AA' or AB stacking. A^-/A peak intensity ratio fluctuation can be observed in both AA' and AB stacked bilayer samples. As such, it is not an identifying feature of the stacking order. In search for the physical origin of the observed fluctuation of A^-/A peak ratio in PL, we note two features unique to our Au tipped surfaces. The first one is the tensor nature of the plasmonic surface.

Plasmon resonance transforms the TE mode of the excitation light of near perpendicular incidence (with the electric field vector being coplanar with MoS_2 layers) into local EM field with the out-of-plane electric field being comparable to the in-plane field (Figure 5.4(b)). The out-of-plane electric field component contributes to symmetry breaking that could lead to noticeable changes in the luminescence behavior of especially the symmetric AA' stacked islands. The second feature is the difference in electron affinity between Au (2.308 eV)[104] and bilayer MoS_2 (4.0-4.2 eV)[105-107] leading to an effective n-type doping of MoS_2.[108] Considering the Au and the MoS_2 as two equal potential bodies, the electron density in MoS_2 will be dependent on the distance between it and the underlying Au surface, which in turn varies with location due to the imperfection in our nano-fabrication. The exciton and trion luminescence peak intensity are known to depend sensitively and differently on the local carrier density.[102] This we believe is the reason for the variation observed in the A^-/A peak ratio.

It can also be noticed that there is a slight blue shift of the A-peak from the monolayer and bilayer MoS_2 on Au pyramid region compared with those on flat Au region and on SiO_2/Si substrate. The origin of the blue shift cannot be explained by the static electric field due to the electron transfer from Au to MoS_2 because of the red shift predicted by DFT simulation.[109, 110] There are two main differences in the physical environment of MoS_2 over Au pyramids compared to that over flat Au: the tensile strain in MoS_2 due to the non-planar topology of the Au pyramids, and the significant out-of-plane EM field due to plasmon resonance. The former is unlikely to be

the primary cause based on the previous experimental observations of tensile strain leading to PL red shift.[111, 112] By the process of elimination, we believe that the primary cause of the A-peak blue shift is the intense out-of-plane EM field from plasmon resonance. Further study is needed to confirm this point.

Considering the growing interest in valleytronics in TMD materials, the interlayer stacking order is definitely a key variable which should be considered when developing valleytronics technology. It has been proven that AB stacked bilayer MoS_2 can provide more robust valley polarization than that of AA' stacked bilayer due to the non-centro-symmetry.[74] Therefore, one primary concern is to control the fabrication so that only one type (AB stacking) of stacking is present. AA' stacked (2H phase) MoS_2 is dominant and more stable in nature. 3R MoS_2 has been shown to transform to 2H MoS_2 at elevated temperatures.[113] The histogram of our CVD grown samples shows that AA' stacked bilayer islands outnumbering that of AB stacked bilayer by almost 50% (~370 over ~250 as in Figure 5.10). DFT calculation also indicates that AA' stacked bilayer MoS_2 has relatively lower ground-state total energy than AB stacked bilayer.[77] It is apparent that the ability of fabricating exclusively AB stacked bilayer MoS_2 appears to be a fundamental challenge and requires in depth understanding of the most manufacturably fabrication technology, CVD.

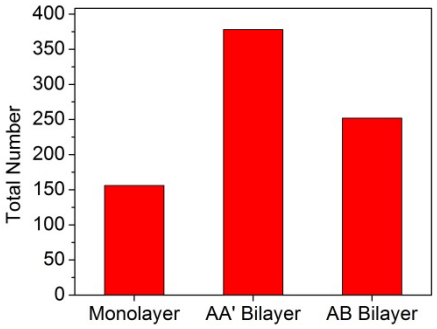

Figure 5.10 Histogram of CVD grown monolayer, AA’ and AB stacked bilayer MoS_2.

5.4 Conclusion

We have demonstrated that the CVD grown AA’ (60° stacking) and AB (0° stacking) stacked bilayer MoS_2 have distinct properties in terms of Raman and PL using Au nano-pyramid plasmonic substrates. The “a” peak appears in AA’ stacked bilayer MoS_2 resonance Raman spectra but not in AB stacked bilayer, a feature that can be used as a Raman finger print to differentiate the two types of bilayer MoS_2. The lower indirect gap energy indicates that AB stacked bilayer MoS_2 has stronger inter-layer electronic coupling than AA’ stacked bilayer. In addition to revealing the subtle differences in AA’ and AB stacked bilayer MoS_2, the results establish three methods for distinguishing between the two stacking orders, namely, optical microscopy, SERS, and PL.

Chapter 6 Summary and Future Study

6.1 Summary

This dissertation discusses the capability limit of the SERS fiber technology, and proposes strategies to enhance the Raman signal intensity and the spatial resolution. A serendipitous discovery of bilayer MoS_2 Raman and photoluminescence spectral features is also presented in the dissertation. The following is a summary of the dissertation work presented:

In Chapter 2, Au nanotriangle array based SERS fiber probe has been fabricate and the factors affecting the Raman signal through fiber are investigated. These factors include N.A. of optical lens, slit width, fiber length and SERS array size on fiber facet. Raman signal can be enhanced through matching the N.A. of lens to the N.A. of fiber and matching of the slit width to the size of the enlarged fiber core image. The Raman signal intensity appears to be independent of the fiber length up to several meters but the S/N will decrease with fiber length. Size of SERS array coated on fiber facet is one primary factor account for the Raman signal loss, which is ultimately due to the decrease in laser power density on the fiber end. The most fundamental optimization consideration for SERS fiber probe is the tradeoff between sensitivity and spatial resolution. SERS fiber probe with hybrid graphene/Au nanoarray is also fabricated and is found to be superior to the fiber probe with bare Au nanoarray in terms of the sensitivity.

Chapter 3 presents FDTD simulation of electrical field of a novel Au nanostructure for the enhancement and spatial confinement of the electric field. We demonstrate a Au pyramid/ring

SERS platform with enhancement of the spatial confinement of the electric field for potential SERS fiber probe application. Excitation of SPPs by circular Au rings and coupling of SPPs with Au pyramids are studied to improve the electric field and the overall SERS enhancement of the platform. By combination of Au pyramids with Au rings, the hot spot volume as well as electric filed intensity at hot spots around Au pyramid are increased significantly compared with bare Au pyramids array. It is also found out that the more pyramid overlaps with the SPP focal centers, the higher coupling efficiency can be achieved, therefore leading to more hot spots and higher electric field enhancement. The electric field enhancement up to 140× can be achieved and the anticipated SERS signal enhancement of up to 8 orders of magnitude. The results of simulation with back light illumination demonstrate that the thickness of Au film substrates plays a significant role for the signal extracting from backside when the SERS platform are transferred onto a fiber facet. Highest electric field enhancement can be achieved without the Au film for fiber application. Au pyramids combined with rings could achieve the confinement of the electric field within a 700×700 nm region, which could provide higher spatial resolution for SERS fiber probe.

Chapter 4 presents a systematic study on a practical way of patterning metallic nanostructures for achieving high SERS EFs and high hot spot density. By superimposing one layer Au triangle array on another to form multilayer triangle array, SERS signal can be enhanced by two orders of magnitude. We also develop the physical understanding of the SERS

enhancement of multilayer triangle array. The drastic increased SERS EFs and the hot spot density are due to the increase in the amount of gaps formed between Au triangles and the decrease in the gap size. The optimum layer number for Au triangle array studied in this work is 4 layers through FDTD simulation and theoretical analysis. The patterning method proposed can be used to form multilayer nanoarray with other shapes in order to achieve ultra-strong local electromagnetic field.

In Chapter 5, we report the serendipitous discovery about bilayer MoS_2 spectral features when exploring the use of MoS_2 as a potential SERS enhancement substrate. We have demonstrated that the CVD grown AA' (60° stacking) and AB (0° stacking) stacked bilayer MoS_2 have distinct properties in terms of Raman and PL using Au nanopyramid plasmonic substrates. The "a" peak appears in AA' stacked bilayer MoS_2 resonance Raman spectra but not in AB stacked bilayer, a feature that can be used as a Raman finger print to differentiate the two types of bilayer MoS_2. The lower indirect gap energy indicates that AB stacked bilayer MoS_2 has stronger inter-layer electronic coupling than AA' stacked bilayer. In addition to revealing the subtle differences in AA' and AB stacked bilayer MoS_2, our results establish three methods for distinguishing between the two stacking orders, namely, optical microscopy, SERS, and PL.

6.2 Direction of Future Study

SERS fiber probe based on Au nanotriangle array has been successfully fabricated and the factors that affect the Raman signal through fiber have been investigated. To extend the SERS

fiber techniques to practical clinical application, many efforts are required to improve the performance of the SERS fiber probe. In this section, some of the future research direction will be discussed.

6.2.1 Optimization of SRES Substrate

Compared with free-space SERS technique, SERS fiber probe suffers from Raman signal loss mainly due to the coupling between fiber and lens. A highly sensitive SERS substrate which can be integrated on fiber facet is the key to guarantee the performance of SERS fiber probe. Au triangle array has been demonstrated to be a good SERS substrate for SERS fiber and shows reasonable SERS performance (10^{-6} M detection limit for R6G solution). However, there is still room for improvement.

SERS substrate used for fiber probe should be sensitive enough to offset the signal loss due to fiber coupling, and yet should be reasonably transparent to let the Raman scattered light pass through. FDTD simulation is a perfect tool to design the SERS substrates for fiber application. There are several factors need to be concerned when designing the SERS substrates. The first one is the choice of SERS materials. Au and Ag are the two major metals for SERS substrates. Ag nanostructure commonly can provide stronger LSPR effect than Au in the visible wavelength range and thus can generate stronger SERS effect than Au. However, Ag is easily to be oxidized in ambient environment and may not be bio-compatible when exposed to tissues. Combining graphene and Ag to form a hybrid SERS structure is an alternative way to take advantage of the

strong SERS effect of Ag nanostructure. The second factor is the tradeoff between the area of SERS substrates and the SERS EF. The area here means the projected area of SERS structure on fiber facet. The fiber core area should not be fully covered in order to collect the Raman scattered light.

6.2.2 Spatial Resolution of SERS Fiber Probe

Spatial resolution for SERS fiber probe means the size of the Raman signal source. For typical SERS fiber probe, the spatial resolution is similar to its fiber core size because only the Raman scattered light generated close to the fiber core can be collected and transmitted to the spectrometer. In this dissertation, a metal film with an opening window in the center is coated on fiber facet to confine the size of signal source and thus improve the spatial resolution of SERS fiber probe up to 10 μm. Using the similar method, spatial resolution can be further enhanced by shrinking the size of the opening window. Challenge of this method is that the Raman signal intensity drops as the opening window size decreases. To overcome the signal loss due to the reduced SERS region, SERS EF of the substrates needs to be improved so that collected Raman signal is still discernable under high spatial resolution. Another direction is to pull fiber to a tapered shape to improve the spatial resolution.[114, 115] By pulling the optical fiber with a fiber puller, a fiber tip with diameter less than 100 nm can be fabricated. SERS fiber probe combined with such a tapered fiber and SERS nanostructure has the potential to probe the bio-information within submicron sized region.

Bibliography

1. Le Ru, E. C.; Etchegoin, P. G. Single-molecule surface-enhanced Raman spectroscopy. *Annual Review of Physical Chemistry* 2012, 63, 65-87.

2. Kneipp, J.; Kneipp, H.; Kneipp, K. SERS - a single-molecule and nanoscale tool for bioanalytics. *Chemical Society Reviews* 2008, 37, 1052-1060.

3. Stiles, P. L.; Dieringer, J. A.; Shah, N. C.; Van Duyne, R. R. Surface-Enhanced Raman Spectroscopy. In *Annual Review of Analytical Chemistry*, 2008; Vol. 1, pp 601-626.

4. Fleischmann, M.; Hendra, P. J.; McQuillan, A. Raman spectra of pyridine adsorbed at a silver electrode. *Chemical Physics Letters* 1974, 26, 163-166.

5. Wang, P.; Liang, O.; Zhang, W.; Schroeder, T.; Xie, Y. H. Ultra‐Sensitive Graphene‐Plasmonic Hybrid Platform for Label‐Free Detection. *Advanced Materials* 2013, 25, 4918-4924.

6. Wang, P.; Xia, M.; Liang, O.; Sun, K.; Cipriano, A. F.; Schroeder, T.; Liu, H.; Xie, Y.-H. Label-Free SERS Selective Detection of Dopamine and Serotonin Using Graphene-Au Nanopyramid Heterostructure. *Analytical Chemistry* 2015, 87, 10255-10261.

7. Huang, J.-A.; Zhao, Y.-Q.; Zhang, X.-J.; He, L.-F.; Wong, T.-L.; Chui, Y.-S.; Zhang, W.-J.; Lee, S.-T. Ordered Ag/Si nanowires array: wide-range surface-enhanced Raman spectroscopy for reproducible biomolecule detection. *Nano letters* 2013, 13, 5039-5045.

8. Li, L.; Hutter, T.; Steiner, U.; Mahajan, S. Single molecule SERS and detection of

biomolecules with a single gold nanoparticle on a mirror junction. *Analyst* 2013, 138, 4574-4578.

9. Li, J. F.; Huang, Y. F.; Ding, Y.; Yang, Z. L.; Li, S. B.; Zhou, X. S.; Fan, F. R.; Zhang, W.; Zhou, Z. Y.; Ren, B. Shell-isolated nanoparticle-enhanced Raman spectroscopy. *nature* 2010, 464, 392-395.

10. Cho, W. J.; Kim, Y.; Kim, J. K. Ultrahigh-density array of silver nanoclusters for SERS substrate with high sensitivity and excellent reproducibility. *ACS nano* 2011, 6, 249-255.

11. McVeigh, P. Z.; Mallia, R. J.; Veilleux, I.; Wilson, B. C. Development of a widefield SERS imaging endoscope. *Proceedings of the SPIE - The International Society for Optical Engineering* 2012, 8217, 821704 (6 pp.)-821704 (6 pp.).

12. Lucotti, A.; Zerbi, G. Fiber-optic SERS sensor with optimized geometry. *Sensors and Actuators B-Chemical* 2007, 121, 356-364.

13. Gessner, R.; Rösch, P.; Petry, R.; Schmitt, M.; Strehle, M.; Kiefer, W.; Popp, J. The application of a SERS fiber probe for the investigation of sensitive biological samples. *Analyst* 2004, 129, 1193-1199.

14. Stoddart, P. R.; White, D. J. Optical fibre SERS sensors. *Analytical and Bioanalytical Chemistry* 2009, 394, 1761-1774.

15. Willets, K. A.; Van Duyne, R. P. Localized surface plasmon resonance spectroscopy and sensing. In *Annual review of physical chemistry*, 2007; Vol. 58, pp 267-297.

16. Haes, A. J.; Van Duyne, R. P. A unified view of propagating and localized surface plasmon

resonance biosensors. *Analytical and bioanalytical chemistry* 2004, 379, 920-930.

17. Le Ru, E.; Etchegoin, P. *Principles of Surface-Enhanced Raman Spectroscopy: and related plasmonic effects*. Elsevier: 2008.

18. Fang, J.; Yi, Y.; Ding, B.; Song, X. A route to increase the enhancement factor of surface enhanced Raman scattering (SERS) via a high density Ag flower-like pattern. *Applied Physics Letters* 2008, 92, 131115.

19. Xiong, Y.; McLellan, J. M.; Chen, J.; Yin, Y.; Li, Z.-Y.; Xia, Y. Kinetically controlled synthesis of triangular and hexagonal nanoplates of palladium and their SPR/SERS properties. *Journal of the American Chemical Society* 2005, 127, 17118-17127.

20. Xie, J.; Zhang, Q.; Lee, J. Y.; Wang, D. I. The synthesis of SERS-active gold nanoflower tags for in vivo applications. *ACS nano* 2008, 2, 2473-2480.

21. Camden, J. P.; Dieringer, J. A.; Wang, Y.; Masiello, D. J.; Marks, L. D.; Schatz, G. C.; Van Duyne, R. P. Probing the Structure of Single-Molecule Surface-Enhanced Raman Scattering Hot Spots. *Journal of the American Chemical Society* 2008, 130, 12616-12617.

22. Dasary, S. S.; Singh, A. K.; Senapati, D.; Yu, H.; Ray, P. C. Gold nanoparticle based label-free SERS probe for ultrasensitive and selective detection of trinitrotoluene. *Journal of the American Chemical Society* 2009, 131, 13806-13812.

23. Lu, X.; Rycenga, M.; Skrabalak, S. E.; Wiley, B.; Xia, Y. Chemical synthesis of novel plasmonic nanoparticles. *Annual review of physical chemistry* 2009, 60, 167-192.

24. Bantz, K. C.; Meyer, A. F.; Wittenberg, N. J.; Im, H.; Kurtulus, O.; Lee, S. H.; Lindquist, N. C.; Oh, S.-H.; Haynes, C. L. Recent progress in SERS biosensing. *Physical Chemistry Chemical Physics* 2011, 13, 11551-11567.

25. Stuart, D. A.; Yuen, J. M.; Shah, N.; Lyandres, O.; Yonzon, C. R.; Glucksberg, M. R.; Walsh, J. T.; Van Duyne, R. P. In vivo glucose measurement by surface-enhanced Raman spectroscopy. *Analytical chemistry* 2006, 78, 7211-7215.

26. Qian, X.; Peng, X.-H.; Ansari, D. O.; Yin-Goen, Q.; Chen, G. Z.; Shin, D. M.; Yang, L.; Young, A. N.; Wang, M. D.; Nie, S. In vivo tumor targeting and spectroscopic detection with surface-enhanced Raman nanoparticle tags. *Nature biotechnology* 2008, 26, 83-90.

27. Lane, L. A.; Qian, X.; Nie, S. SERS Nanoparticles in Medicine: From Label-Free Detection to Spectroscopic Tagging. *Chemical Reviews* 2015, 115, 10489-10529.

28. Daniels, J. S.; Pourmand, N. Label-free impedance biosensors: Opportunities and challenges. *Electroanalysis* 2007, 19, 1239-1257.

29. Fan, M.; Wang, P.; Escobedo, C.; Sinton, D.; Brolo, A. G. Surface-enhanced Raman scattering (SERS) optrodes for multiplexed on-chip sensing of nile blue A and oxazine 720. *Lab on a Chip* 2012, 12, 1554-1560.

30. Foti, A.; D'Andrea, C.; Bonaccorso, F.; Lanza, M.; Calogero, G.; Messina, E.; Maragò, O. M.; Fazio, B.; Gucciardi, P. G. A shape-engineered surface-enhanced raman scattering optical fiber sensor working from the visible to the near-Infrared. *Plasmonics* 2013, 8, 13-23.

31. Smythe, E. J.; Dickey, M. D.; Bao, J.; Whitesides, G. M.; Capasso, F. Optical antenna arrays on a fiber facet for in situ surface-enhanced Raman scattering detection. *Nano letters* 2009, 9, 1132-1138.

32. Association, A. s. 2012 Alzheimer's disease facts and figures. *Alzheimer's & Dementia* 2012, 8, 131-168.

33. Murphy, M. P.; LeVine, H., III. Alzheimer's Disease and the Amyloid-beta Peptide. *Journal of Alzheimers Disease* 2010, 19, 311-323.

34. Hardy, J.; Selkoe, D. J. Medicine - The amyloid hypothesis of Alzheimer's disease: Progress and problems on the road to therapeutics. *Science* 2002, 297, 353-356.

35. Heien, M. L.; Khan, A. S.; Ariansen, J. L.; Cheer, J. F.; Phillips, P. E.; Wassum, K. M.; Wightman, R. M. Real-time measurement of dopamine fluctuations after cocaine in the brain of behaving rats. *Proceedings of the National Academy of Sciences of the United States of America* 2005, 102, 10023-10028.

36. Phillips, P. E.; Stuber, G. D.; Heien, M. L.; Wightman, R. M.; Carelli, R. M. Subsecond dopamine release promotes cocaine seeking. *Nature* 2003, 422, 614-618.

37. Xu, W.; Ling, X.; Xiao, J.; Dresselhaus, M. S.; Kong, J.; Xu, H.; Liu, Z.; Zhang, J. Surface enhanced Raman spectroscopy on a flat graphene surface. *Proceedings of the National Academy of Sciences* 2012, 109, 9281-9286.

38. Ling, X.; Fang, W.; Lee, Y.-H.; Araujo, P. T.; Zhang, X.; Rodriguez-Nieva, J. F.; Lin, Y.;

Zhang, J.; Kong, J.; Dresselhaus, M. S. Raman Enhancement Effect on Two-Dimensional Layered Materials: Graphene, h-BN and MoS2. *Nano Letters* 2014, 14, 3033-3040.

39. Xu, W.; Mao, N.; Zhang, J. Graphene: A Platform for Surface-Enhanced Raman Spectroscopy. *Small* 2013, 9, 1206-1224.

40. Samanta, A.; Maiti, K. K.; Soh, K. S.; Liao, X.; Vendrell, M.; Dinish, U.; Yun, S. W.; Bhuvaneswari, R.; Kim, H.; Rautela, S. Ultrasensitive Near‐Infrared Raman Reporters for SERS‐Based In Vivo Cancer Detection. *Angewandte Chemie International Edition* 2011, 50, 6089-6092.

41. Kennedy, R. T. Emerging trends in in vivo neurochemical monitoring by microdialysis. *Current opinion in chemical biology* 2013, 17, 860-867.

42. Siksou, L.; Rostaing, P.; Lechaire, J.-P.; Boudier, T.; Ohtsuka, T.; Fejtová, A.; Kao, H.-T.; Greengard, P.; Gundelfinger, E. D.; Triller, A. Three-dimensional architecture of presynaptic terminal cytomatrix. *The Journal of neuroscience* 2007, 27, 6868-6877.

43. Wang, P.; Zhang, W.; Liang, O.; Pantoja, M.; Katzer, J.; Schroeder, T.; Xie, Y. H. Giant Optical Response from Graphene-Plasmonic System. *ACS Nano* 2012, 6, 6244-6249.

44. Kong Chong, C.; Shen, C.; Fong, Y.; Zhu, J.; Yan, F.-X.; Brush, S.; Mann, C. K.; Vickers, T. J. Raman spectroscopy with a fiber-optic probe. *Vibrational spectroscopy* 1992, 3, 35-45.

45. Liu, K.; Zhang, J.-J.; Cheng, F.-F.; Zheng, T.-T.; Wang, C.; Zhu, J.-J. Green and facile synthesis of highly biocompatible graphene nanosheets and its application for cellular imaging and

drug delivery. *Journal of Materials Chemistry* 2011, 21, 12034-12040.

46. Liu, Y.; Yu, D.; Zeng, C.; Miao, Z.; Dai, L. Biocompatible Graphene Oxide-Based Glucose Biosensors. *Langmuir* 2010, 26, 6158-6160.

47. Kim, Y.-K.; Kim, M.-H.; Min, D.-H. Biocompatible reduced graphene oxide prepared by using dextran as a multifunctional reducing agent. *Chemical Communications* 2011, 47, 3195-3197.

48. Chen, W.; Abeysinghe, D. C.; Nelson, R. L.; Zhan, Q. Plasmonic Lens Made of Multiple Concentric Metallic Rings under Radially Polarized Illumination. *Nano Letters* 2009, 9, 4320-4325.

49. Fang, Z.; Peng, Q.; Song, W.; Hao, F.; Wang, J.; Nordlander, P.; Zhu, X. Plasmonic Focusing in Symmetry Broken Nanocorrals. *Nano Letters* 2011, 11, 893-897.

50. Lerman, G. M.; Yanai, A.; Levy, U. Demonstration of Nanofocusing by the use of Plasmonic Lens Illuminated with Radially Polarized Light. *Nano Letters* 2009, 9, 2139-2143.

51. Liu, Z.; Steele, J. M.; Lee, H.; Zhang, X. Tuning the focus of a plasmonic lens by the incident angle. *Applied physics letters* 2006, 88, 171108.

52. Liu, Z.; Steele, J. M.; Srituravanich, W.; Pikus, Y.; Sun, C.; Zhang, X. Focusing Surface Plasmons with a Plasmonic Lens. *Nano Letters* 2005, 5, 1726-1729.

53. Bahns, J.; Imre, A.; Vlasko-Vlasov, V.; Pearson, J.; Hiller, J.; Chen, L.; Welp, U. Enhanced Raman scattering from focused surface plasmons. *Applied physics letters* 2007, 91, 081104.

54. Tabatabaei, M.; Najiminaini, M.; Davieau, K.; Kaminska, B.; Singh, M. R.; Carson, J. J. L.; Lagugné-Labarthet, F. Tunable 3D Plasmonic Cavity Nanosensors for Surface-Enhanced Raman Spectroscopy with Sub-femtomolar Limit of Detection. *ACS Photonics* 2015, 2, 752-759.

55. Zayats, A. V.; Smolyaninov, II; Maradudin, A. A. Nano-optics of surface plasmon polaritons. *Physics Reports-Review Section of Physics Letters* 2005, 408, 131-314.

56. https://commons.wikimedia.org/wiki/File%3AFDTD_Yee_grid_2d-3d.svg.

57. Barnes, W. L. Surface plasmon–polariton length scales: a route to sub-wavelength optics. *Journal of Optics A: Pure and Applied Optics* 2006, 8, S87.

58. Fang, Y.; Seong, N.-H.; Dlott, D. D. Measurement of the distribution of site enhancements in surface-enhanced Raman scattering. *Science* 2008, 321, 388-392.

59. Liu, D.; Li, C.; Zhou, F.; Zhang, T.; Zhang, H.; Li, X.; Duan, G.; Cai, W.; Li, Y. Rapid Synthesis of Monodisperse Au Nanospheres through a Laser Irradiation -Induced Shape Conversion, Self-Assembly and Their Electromagnetic Coupling SERS Enhancement. *Scientific Reports* 2015, 5, 7686.

60. Hulteen, J. C.; Treichel, D. A.; Smith, M. T.; Duval, M. L.; Jensen, T. R.; Van Duyne, R. P. Nanosphere lithography: size-tunable silver nanoparticle and surface cluster arrays. *The Journal of Physical Chemistry B* 1999, 103, 3854-3863.

61. Zhang, H.; Liu, M.; Zhou, F.; Liu, D.; Liu, G.; Duan, G.; Cai, W.; Li, Y. Physical Deposition Improved SERS Stability of Morphology Controlled Periodic Micro/Nanostructured Arrays Based

on Colloidal Templates. *Small* 2015, 11, 844-853.

62. Haynes, C. L.; Van Duyne, R. P. Nanosphere lithography: a versatile nanofabrication tool for studies of size-dependent nanoparticle optics. *The Journal of Physical Chemistry B* 2001, 105, 5599-5611.

63. Zhang, H.; Zhou, F.; Liu, M.; Liu, D.; Men, D.; Cai, W.; Duan, G.; Li, Y. Spherical Nanoparticle Arrays with Tunable Nanogaps and Their Hydrophobicity Enhanced Rapid SERS Detection by Localized Concentration of Droplet Evaporation. *Advanced Materials Interfaces* 2015.

64. Gui, J. Y.; Stern, D. A.; Frank, D. G.; Lu, F.; Zapien, D. C.; Hubbard, A. T. Adsorption and surface structural chemistry of thiophenol, benzyl mercaptan, and alkyl mercaptans. Comparative studies at silver (111) and platinum (111) electrodes by means of Auger spectroscopy, electron energy loss spectroscopy, low energy electron diffraction and electrochemistry. *Langmuir* 1991, 7, 955-963.

65. Wan, L.-J.; Terashima, M.; Noda, H.; Osawa, M. Molecular orientation and ordered structure of benzenethiol adsorbed on gold (111). *The Journal of Physical Chemistry B* 2000, 104, 3563-3569.

66. Xia, M.; Zhang, P.; Qiao, K.; Bai, Y.; Xie, Y.-H. Coupling SPP with LSPR for Enhanced Field Confinement: A Simulation Study. *The Journal of Physical Chemistry C* 2016, 120, 527–533.

67. Merk, V.; Kneipp, J.; Leosson, K. Gap size reduction and increased SERS enhancement in

lithographically patterned nanoparticle arrays by templated growth. *Advanced Optical Materials* 2013, 1, 313-318.

68. Li, H.; Cullum, B. M. Dual layer and multilayer enhancements from silver film over nanostructured surface-enhanced raman substrates. *Applied spectroscopy* 2005, 59, 410-417.

69. Li, H.; Baum, C. E.; Sun, J.; Cullum, B. M. Multilayer enhanced gold film over nanostructure surface-enhanced Raman substrates. *Applied spectroscopy* 2006, 60, 1377-1385.

70. Mak, K. F.; Lee, C.; Hone, J.; Shan, J.; Heinz, T. F. Atomically thin MoS 2: a new direct-gap semiconductor. *Physical Review Letters* 2010, 105, 136805.

71. Eda, G.; Yamaguchi, H.; Voiry, D.; Fujita, T.; Chen, M.; Chhowalla, M. Photoluminescence from chemically exfoliated MoS2. *Nano Letters* 2011, 11, 5111-5116.

72. Splendiani, A.; Sun, L.; Zhang, Y.; Li, T.; Kim, J.; Chim, C.-Y.; Galli, G.; Wang, F. Emerging photoluminescence in monolayer MoS2. *Nano Letters* 2010, 10, 1271-1275.

73. Xiao, D.; Liu, G.-B.; Feng, W.; Xu, X.; Yao, W. Coupled spin and valley physics in monolayers of MoS 2 and other group-VI dichalcogenides. *Physical Review Letters* 2012, 108, 196802.

74. Suzuki, R.; Sakano, M.; Zhang, Y.; Akashi, R.; Morikawa, D.; Harasawa, A.; Yaji, K.; Kuroda, K.; Miyamoto, K.; Okuda, T. Valley-dependent spin polarization in bulk MoS2 with broken inversion symmetry. *Nature nanotechnology* 2014, 9, 611-617.

75. Zeng, H.; Dai, J.; Yao, W.; Xiao, D.; Cui, X. Valley polarization in MoS2 monolayers by

optical pumping. *Nature nanotechnology* 2012, 7, 490-493.

76. Mak, K. F.; He, K.; Shan, J.; Heinz, T. F. Control of valley polarization in monolayer MoS2 by optical helicity. *Nature nanotechnology* 2012, 7, 494-498.

77. He, J.; Hummer, K.; Franchini, C. Stacking effects on the electronic and optical properties of bilayer transition metal dichalcogenides MoS 2, MoSe 2, WS 2, and WSe 2. *Physical Review B* 2014, 89, 075409.

78. Li, H.; Zhang, Q.; Yap, C. C. R.; Tay, B. K.; Edwin, T. H. T.; Olivier, A.; Baillargeat, D. From bulk to monolayer MoS2: evolution of Raman scattering. *Advanced Functional Materials* 2012, 22, 1385-1390.

79. Wu, S.; Ross, J. S.; Liu, G.-B.; Aivazian, G.; Jones, A.; Fei, Z.; Zhu, W.; Xiao, D.; Yao, W.; Cobden, D. Electrical tuning of valley magnetic moment through symmetry control in bilayer MoS2. *Nature Physics* 2013, 9, 149-153.

80. Zeng, H.; Liu, G.-B.; Dai, J.; Yan, Y.; Zhu, B.; He, R.; Xie, L.; Xu, S.; Chen, X.; Yao, W. Optical signature of symmetry variations and spin-valley coupling in atomically thin tungsten dichalcogenides. *Scientific reports* 2013, 3.

81. Gong, Z.; Liu, G.-B.; Yu, H.; Xiao, D.; Cui, X.; Xu, X.; Yao, W. Magnetoelectric effects and valley-controlled spin quantum gates in transition metal dichalcogenide bilayers. *Nature communications* 2013, 4.

82. Xu, X.; Yao, W.; Xiao, D.; Heinz, T. F. Spin and pseudospins in layered transition metal

dichalcogenides. *Nature Physics* 2014, 10, 343-350.

83. Anghel, S.; Chumakov, Y.; Kravtsov, V.; Mitioglu, A.; Plochocka, P.; Sushkevich, K.; Volodina, G.; Colev, A.; Kulyuk, L. Identification of 2H and 3R polytypes of MoS2 layered crystals using photoluminescence spectroscopy. *arXiv preprint arXiv:1411.3850* 2014.

84. Livneh, T.; Spanier, J. E. A Comprehensive Spectral Analysis of Multiphonon Resonant Raman Scattering in 2H-MoS2. *arXiv preprint arXiv:1408.6748* 2014.

85. Jiang, T.; Liu, H.; Huang, D.; Zhang, S.; Li, Y.; Gong, X.; Shen, Y.-R.; Liu, W.-T.; Wu, S. Valley and band structure engineering of folded MoS2 bilayers. *Nat Nano* 2014, 9, 825-829.

86. van der Zande, A. M.; Kunstmann, J.; Chernikov, A.; Chenet, D. A.; You, Y.; Zhang, X.; Huang, P. Y.; Berkelbach, T. C.; Wang, L.; Zhang, F. Tailoring the electronic structure in bilayer molybdenum disulfide via interlayer twist. *Nano Letters* 2014, 14, 3869-3875.

87. Huang, S.; Ling, X.; Liang, L.; Kong, J.; Terrones, H.; Meunier, V.; Dresselhaus, M. S. Probing the Interlayer Coupling of Twisted Bilayer MoS2 Using Photoluminescence Spectroscopy. *Nano Letters* 2014, 14, 5500-5508.

88. Liu, K.; Zhang, L.; Cao, T.; Jin, C.; Qiu, D.; Zhou, Q.; Zettl, A.; Yang, P.; Louie, S. G.; Wang, F. Evolution of interlayer coupling in twisted molybdenum disulfide bilayers. *Nature communications* 2014, 5.

89. Najmaei, S.; Liu, Z.; Zhou, W.; Zou, X.; Shi, G.; Lei, S.; Yakobson, B. I.; Idrobo, J.-C.; Ajayan, P. M.; Lou, J. Vapour phase growth and grain boundary structure of molybdenum

disulphide atomic layers. *Nature materials* 2013, 12, 754-759.

90. Oh, J. R.; Moon, J. H.; Yoon, S.; Park, C. R.; Do, Y. R. Fabrication of wafer-scale polystyrene photonic crystal multilayers via the layer-by-layer scooping transfer technique. *Journal of Materials Chemistry* 2011, 21, 14167-14172.

91. Yang, S.; Kang, J.; Yue, Q.; Yao, K. Vapor Phase Growth and Imaging Stacking Order of Bilayer Molybdenum Disulfide. *The Journal of Physical Chemistry C* 2014, 118, 9203-9208.

92. Koch, C. T. *Determination of core structure periodicity and point defect density along dislocations*. 2002.

93. Zhou, W.; Lee, J.; Nanda, J.; Pantelides, S. T.; Pennycook, S. J.; Idrobo, J.-C. Atomically localized plasmon enhancement in monolayer graphene. *Nat Nano* 2012, 7, 161-165.

94. Ferrari, A. C.; Meyer, J. C.; Scardaci, V.; Casiraghi, C.; Lazzeri, M.; Mauri, F.; Piscanec, S.; Jiang, D.; Novoselov, K. S.; Roth, S.; Geim, A. K. Raman spectrum of graphene and graphene layers. *Physical Review Letters* 2006, 97.

95. Lee, C.; Yan, H.; Brus, L. E.; Heinz, T. F.; Hone, J.; Ryu, S. Anomalous lattice vibrations of single-and few-layer MoS2. *ACS nano* 2010, 4, 2695-2700.

96. Chakraborty, B.; Matte, H.; Sood, A.; Rao, C. Layer‐dependent resonant Raman scattering of a few layer MoS2. *Journal of Raman Spectroscopy* 2013, 44, 92-96.

97. Scheuschner, N.; Gillen, R.; Staiger, M.; Maultzsch, J. Newly observed first-order resonant Raman modes in few-layer MoS2. *arXiv preprint arXiv:1503.08980* 2015.

98. Sekine, T.; Uchinokura, K.; Nakashizu, T.; Matsuura, E.; Yoshizaki, R. Dispersive Raman mode of layered compound 2H-MoS2 under the resonant condition. *Journal of the Physical Society of Japan* 1984, 53, 811-818.

99. Livneh, T.; Sterer, E. Resonant Raman scattering at exciton states tuned by pressure and temperature in 2 H-MoS 2. *Physical Review B* 2010, 81, 195209.

100. Gołasa, K.; Grzeszczyk, M.; Leszczyński, P.; Faugeras, C.; Nicolet, A.; Wysmołek, A.; Potemski, M.; Babiński, A. Multiphonon resonant Raman scattering in MoS2. *Applied Physics Letters* 2014, 104, 092106.

101. Zhang, Z. M.; Chen, S.; Liang, Y. Z.; Liu, Z. X.; Zhang, Q. M.; Ding, L. X.; Ye, F.; Zhou, H. An intelligent background‐correction algorithm for highly fluorescent samples in Raman spectroscopy. *Journal of Raman Spectroscopy* 2010, 41, 659-669.

102. Mak, K. F.; He, K.; Lee, C.; Lee, G. H.; Hone, J.; Heinz, T. F.; Shan, J. Tightly bound trions in monolayer MoS2. *Nature materials* 2013, 12, 207-211.

103. Schönfeld, B.; Huang, J.; Moss, S. Anisotropic mean-square displacements (MSD) in single-crystals of 2H-and 3R-MoS2. *Acta Crystallographica Section B: Structural Science* 1983, 39, 404-407.

104. Andersen, T.; Haugen, H.; Hotop, H. Binding energies in atomic negative ions: III. *Journal of Physical and Chemical Reference Data* 1999, 28, 1511-1533.

105. Han, S.; Kwon, H.; Kim, S. K.; Ryu, S.; Yun, W. S.; Kim, D.; Hwang, J.; Kang, J.-S.;

Baik, J.; Shin, H. Band-gap transition induced by interlayer van der Waals interaction in MoS 2. *Physical Review B* 2011, 84, 045409.

106. Choi, M. S.; Lee, G.-H.; Yu, Y.-J.; Lee, D.-Y.; Lee, S. H.; Kim, P.; Hone, J.; Yoo, W. J. Controlled charge trapping by molybdenum disulphide and graphene in ultrathin heterostructured memory devices. *Nature communications* 2013, 4, 1624.

107. Das, S.; Chen, H.-Y.; Penumatcha, A. V.; Appenzeller, J. High performance multilayer MoS2 transistors with scandium contacts. *Nano letters* 2012, 13, 100-105.

108. Fontana, M.; Deppe, T.; Boyd, A. K.; Rinzan, M.; Liu, A. Y.; Paranjape, M.; Barbara, P. Electron-hole transport and photovoltaic effect in gated MoS2 Schottky junctions. *Scientific reports* 2013, 3.

109. Liu, Q.; Li, L.; Li, Y.; Gao, Z.; Chen, Z.; Lu, J. Tuning electronic structure of bilayer MoS2 by vertical electric field: a first-principles investigation. *The Journal of Physical Chemistry C* 2012, 116, 21556-21562.

110. Ramasubramaniam, A.; Naveh, D.; Towe, E. Tunable band gaps in bilayer transition-metal dichalcogenides. *Physical Review B* 2011, 84, 205325.

111. He, K.; Poole, C.; Mak, K. F.; Shan, J. Experimental demonstration of continuous electronic structure tuning via strain in atomically thin MoS2. *Nano letters* 2013, 13, 2931-2936.

112. Conley, H. J.; Wang, B.; Ziegler, J. I.; Haglund Jr, R. F.; Pantelides, S. T.; Bolotin, K. I. Bandgap engineering of strained monolayer and bilayer MoS2. *Nano letters* 2013, 13, 3626-3630.

113. Enyashin, A. N.; Yadgarov, L.; Houben, L.; Popov, I.; Weidenbach, M.; Tenne, R.; Bar-Sadan, M.; Seifert, G. New route for stabilization of 1T-WS2 and MoS2 phases. *The Journal of Physical Chemistry C* 2011, 115, 24586-24591.

114. Scaffidi, J. P.; Gregas, M. K.; Seewaldt, V.; Vo-Dinh, T. SERS-based plasmonic nanobiosensing in single living cells. *Analytical and bioanalytical chemistry* 2009, 393, 1135-1141.

115. Berthelot, J.; Acimovic, S. S.; Juan, M. L.; Kreuzer, M. P.; Renger, J.; Quidant, R. Three-dimensional manipulation with scanning near-field optical nanotweezers. *Nat Nano* 2014, 9, 295-299.